
Article:

Magnus, C., Cooper, D., Ma, L. et al. (1 more author) (2020) Microstructures and intrinsic lubricity of in situ Ti3SiC2–TiSi2–TiC MAX phase composite fabricated by reactive spark plasma sintering (SPS). Wear, 448-449. 203169. ISSN 0043-1648

https://doi.org/10.1016/j.wear.2019.203169

Microstructures and intrinsic lubricity of in situ Ti_3SiC_2–$TiSi_2$–TiC MAX phase composite fabricated by reactive spark plasma sintering (SPS)

Carl Magnus, Daniel Cooper, Le Ma, William M. Rainforth

PII: S0043-1648(19)31548-0

DOI: https://doi.org/10.1016/j.wear.2019.203169

Reference: WEA 203169

To appear in: *Wear*

Received Date: 22 October 2019

Revised Date: 22 December 2019

Accepted Date: 23 December 2019

Please cite this article as: C. Magnus, D. Cooper, L. Ma, W.M. Rainforth, Microstructures and intrinsic lubricity of in situ Ti_3SiC_2–$TiSi_2$–TiC MAX phase composite fabricated by reactive spark plasma sintering (SPS), *Wear* (2020), doi: https://doi.org/10.1016/j.wear.2019.203169.

Microstructures and intrinsic lubricity of in situ Ti_3SiC_2–$TiSi_2$–TiC MAX phase composite fabricated by reactive spark plasma sintering (SPS)

Carl Magnus [1],*, Daniel Cooper [1,2], Le Ma [1] and William M. Rainforth [1]

[1] Department of Materials Science and Engineering, The University of Sheffield, Mappin Street, Sheffield S1 3JD, UK

[2] Seaborg Technologies, Titangade 11, 2200, Copenhagen, Denmark

Abstract

MAX phase composite Ti_3SiC_2–$TiSi_2$–TiC based on the $Ti_{n+1}SiC_n$ system was synthesized by spark plasma sintering (SPS) under vacuum sintering conditions. The microstructural evolution upon synthesis and Vickers indentation contact damaged were characterized using scanning electron microscopy (SEM) and optical microscopy (OM). Tribological behaviour of the SPSed MAX phase composite was investigated under dry sliding ambient conditions for evidence of intrinsic lubricity as well as to understand the influence of second phase TiC particles on the wear behaviour of this composite system. Further, the underlying wear mechanisms was elucidated via detailed analyses of the worn surfaces using Raman spectroscopy, SEM-EDS and transmission electron microscopy (TEM). Exhaustive analyses of the worn surface revealed evidence of solid lubrication. Transition in friction and wear is attributed to change in wear mechanism from tribo-oxidative to deformation-induced wear due to the disruption of the tribofilm architecture.

Keywords: Dry sliding; Microhardness; Frictional heating; Transmission electron microscopy

1. Introduction

Early transition-metal ternary metalloceramics composed of hexagonal nanolaminated layered structure with a chemistry $M_{(n+1)}AX_{(n)}$ configuration have attracted a lot of attention [1, 2]. Since first discovered in the late 1960s, MAX phases have been recently further explored to investigate their synthesis and structure-property relation owing to their unusual set of metals (machinability, stiffness, electrical and thermal conductivities) and ceramics (damage tolerance, thermal stability, oxidation resistance) properties [3, 4]. The MAX phases are so-called because of their general formula where M are mainly group-4, group-5, and group-6 transition metals (mainly Ti, Zr, Hf, V, Nb, Ta, Cr, and Mo), while A is mainly an A-group element from groups 9 (Ir), 10 (Pd), 11 (Cu, Au), 12 (Cd, Zn), 13 (Al, Ga, In, Tl), 14

(Si, Ge, Sn, Pb), 15 (P, As, Sb, Bi), X is either C or N and n = 1 – 3 and possibly higher [1, 5, 6]. Fig. 1 shows some of the elements in the periodic table that forms the $M_{n+1}AX_n$ phases.

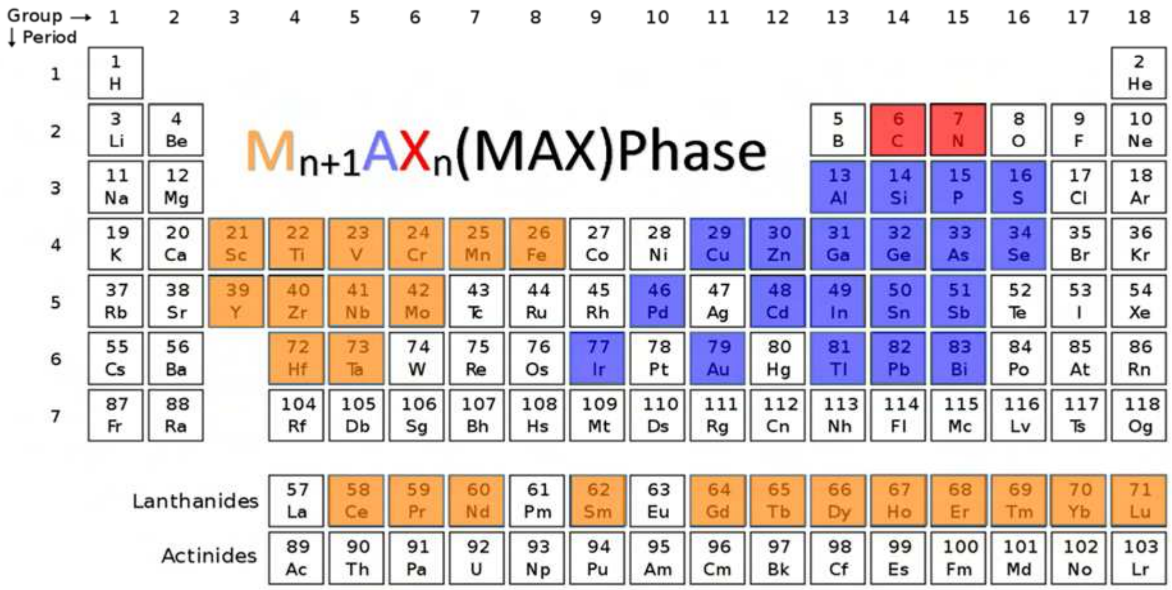

Fig. 1. The periodic table of the M, A, and X elements forming the MAX phases and associated solid-solution MAX phases.

These ternary phases (80 +) crystallize in a hexagonal structure ($P6_3/mmc$ symmetry) with two formula units per unit cell, where $M_{n+1}X_n$ layers are interleaved with pure A-group atoms thus resulting in a characteristic $(M_{n+1}X_n)A(M_{n+1}X_n)A(M_{n+1}X_n)$ crystal structure [7]. The nature of their characteristic layered structure composed of stacking of n "ceramic" interposed with a "metallic" layer [8], coupled with the mixed covalent-metallic nature of the M–X bonds which are exceptionally strong and the relatively weak M–A bonds, endows the MAX phases with their signature mechanical, chemical, and electrical properties [4, 9, 10]. They represent the only class of ceramic-like material that deforms plastically via the nucleation and slip of basal dislocations (BDs) [11, 12] incorporating a series of energy absorbing micro-scale events such as buckling of individual grains, diffuse micro-cracking, delamination of individuals grains, kink and shear band formation followed by eventual grain push-outs and pull-outs [4, 10, 13-20].

Ti_3SiC_2, a 312 compound, is the most studied representative member of the MAX phase family. It possesses unique metalloceramic properties such as low hardness, low density, high modulus, excellent thermal and electrical conductivity, high fracture toughness, damage tolerance and easy machinability [4, 21-23]. Its hexagonal layered crystal structure similar to graphite and MoS_2 [24] suggests it might be an excellent solid lubricant material with a low friction and wear properties suitable in a range of high-temperature structural engineering applications [25, 26]. This is supported by the fact that Ti_3SiC_2 felt lubricious during machining as reported by Barsoum et al. [21]. Numerous research have since been conducted on the tribological behaviour of MAX phases for evidence of lubricity [27]. However, some researchers have reported that albeit Ti_3SiC_2 possessing layered hexagonal crystal structure similar to graphite, it is not intrinsically self-lubricating [28]. This was attributed to a three-body abrasive wear that stems from the fracture and pull-out of the Ti_3SiC_2 grains — representing the dominant wear mechanism at room temperature [27, 29, 30]. The ease of grain fracture and pull-outs has been linked to the weak grain boundary force of the Ti_3SiC_2 grains [31]. In addition, some other authors have highlighted the low hardness and oxidation resistance as the main factors deteriorating the friction and wear properties of monolithic Ti_3SiC_2 [32]. These observations have led to new studies focussing essentially on the incorporation of a second phase hard material in the soft matrix of Ti_3SiC_2 as an effective way to mitigate these weaknesses [32, 33]. Some possible reinforcing materials are TiC and TiB_2 as they possess high hardness, excellent oxidation resistance and close coefficient of thermal expansion with Ti_3SiC_2 [32, 34].

Nevertheless, little is known on the exact wear mechanism(s) as well as the intrinsic self-lubricating behaviour of monolithic Ti_3SiC_2 and Ti_3SiC_2-based material due to the lack of detailed investigation undertaken on the worn surface irrespective of the varying testing conditions reported to date. The scope of this work is to determine comprehensively the wear mechanism sequence of this solid and its associated composites during dry sliding friction at ambient conditions in order to establish the existence of intrinsic self-lubricating behaviour as speculated [30, 35] and to further elucidate their wear mechanism.

2. Experimental procedure

2.1. Powder preparation

Commercially available titanium powder (100 mesh, 99.7 % purity, Aldrich), silicon powder (200 mesh, 99 % purity, Acros organics) and graphite powder were used as starting elemental powders. 5.53 g of titanium powder and 0.98 g of graphite powder were dry-milled in a SPEX 8000 mill continuously for 2 h, which was then subsequently mixed with 1.08 g silicon powder according to a 3:1:2 stoichiometry.

2.2. Consolidation by spark plasma sintering (SPS)

The stoichiometric powder mixture was poured into an electrically and thermally conductive cylindrical graphite mould with an inner diameter of 20 mm. The powder was isolated from the graphite mould and punches by applying a graphite paper previously sprayed with boron nitride (BN) to ease the removal of the sintered sample from the tooling and to further protect graphite dies and punches from possible chemical reaction with the specimen at high temperature. The die was then subsequently covered with graphite felt and tied with graphite wire in order to reduce heat dissipation during the sintering. The sintering cycle was carried out in-situ in vacuum (10^{-2} Pa) in a SPS furnace unit (HP D 25, FCT Systeme GmbH, Rauenstein, Germany). Details of the SPS synthesis, resulting composition and density of the bulk sample is shown in Table 1.

Sample	***Sintering Parameters***				***Density (g/cm^3)***	
	Pressure (MPa)	Temperature (°C)	Heating Rate (°C/min)	Hold Time (min.)	Actual	Relative
80 % Ti_3SiC_2 / 14% TiC / 6% $TiSi_2$	50	1350	50	15	4.437	98 %

Table 1. *Composition, sintering parameters and density of sample sintered by SPS*

2.3. Microstructure characterization

The as-synthesized SPSed disc (Ø = 20 mm) was ground and polished down to 0.5 µm using a diamond paste to ensure the complete removal of the graphite layer surrounding the surface after the SPS synthesis. The resultant polished disc surface was analysed by x-ray diffractometry using a Bruker diffractometer (D2 Phaser Bruker AXS, Karlsruhe, Germany) with a Cu Kα radiation source using a step size of 0.02° and time per step of 3 sec with diffractometer angle range between $2\Theta = 5°$ to $2\Theta = 80°$. Analysis of the XRD pattern was done with Diffract EVA software. Apparent density was measured by employing the Archimedes water immersion technique. The relative density was determined as a percentage of theoretical density upon determination of the phase fractions by Rietveld refinement of the X-ray diffraction data using GSAS and EXPGUI. The residual values of the refinement (R-weighted pattern (R_{wp}); residual of least-squares (R_p); goodness-of-fit (χ^2)) were evaluated. Scanning electron microscopy (SEM) coupled with an EDS detector (Inspect F50, FEI Company, The Netherlands / X-Max AZtec-Nanoanalyis, Oxford Instruments, UK) and transmission electron microscopy (TEM) (Philips EM420 operating at 120 kV/JEOL JEM-F200) were used for microstructural characterization of the pristine sample as well as the post-mortem worn surfaces of the disc. Electron transparent TEM samples were prepared in situ by focused ion beam (FIB) (FEI Helios NanoLab G3 UC, FEI Company, The Netherlands). TEM samples were obtained from the worn surface by preparing FIB cross-sections perpendicular to the sliding direction (across the wear track). Furthermore, point analysis of the evolved chemistry at the worn surface was investigated ex situ by employing a Si-calibrated inVia Renishaw Raman spectrometer (Renishaw plc, UK) with an Ar laser (λ = 514.5 nm, laser output power 20 mW and spot size of 2 μm).

2.4. Hardness and Tribological Testing

Vickers microhardness was measured by indenting the polished surface (Ra = 0.020 μm) of the sintered sample with a microhardness tester (DuraScan 50, ecos Workflow, EMCO-TEST, GmbH) using an indentation load of 4.9 N and a dwell time of 10 s. The indentation load was further increased in order to analyse the resulting change in the indentation zones deformation microstructure. Tribological investigation was undertaken by employing Al_2O_3 ball (99 % GD-25 Alumina Spheric Trafalgar, UK) as counterface using a ball-on-disk tribometer (Model CETR UMT-1, USA) under dry sliding ambient test condition (25 °C/22% RH). An Al_2O_3 ball was used as the counterface due to its relative inertness, as it would not be expected to react with the bulk sample. Normal load was kept constant at 0.5 N and disc rotational speed varied at 50 rpm for 60 min and 100 rpm for 30 min, respectively for each test. Low sliding speed and normal load were used to minimize frictional heating due to the dry sliding test condition. Furthermore, the chosen load is in agreement with an earlier work by Souchet et al. [30] and ensures that the test falls within the friction transition region. A schematic diagram of the ball-on-disc rotational wear test configuration is shown in Fig. 2. The coefficient of friction values reported were continuously recorded by the tribometer during the entire duration of the test. Profiles of the wear scars were measured by taking several profilometric scans and the average taken, so as to determine the wear volume as $V = AL$ (where A refers to the wear scar area determined by its profile and L is the length of track (2□R). The specific wear rate, which is the measure of wear volume per unit distance and per unit load was then determined thus:

$$K = V/F_n.S_d$$

Where K = specific wear rate (mm^3/Nm), V = wear volume (mm^3), F_n = load (N) and S_d = sliding distance (m), respectively.

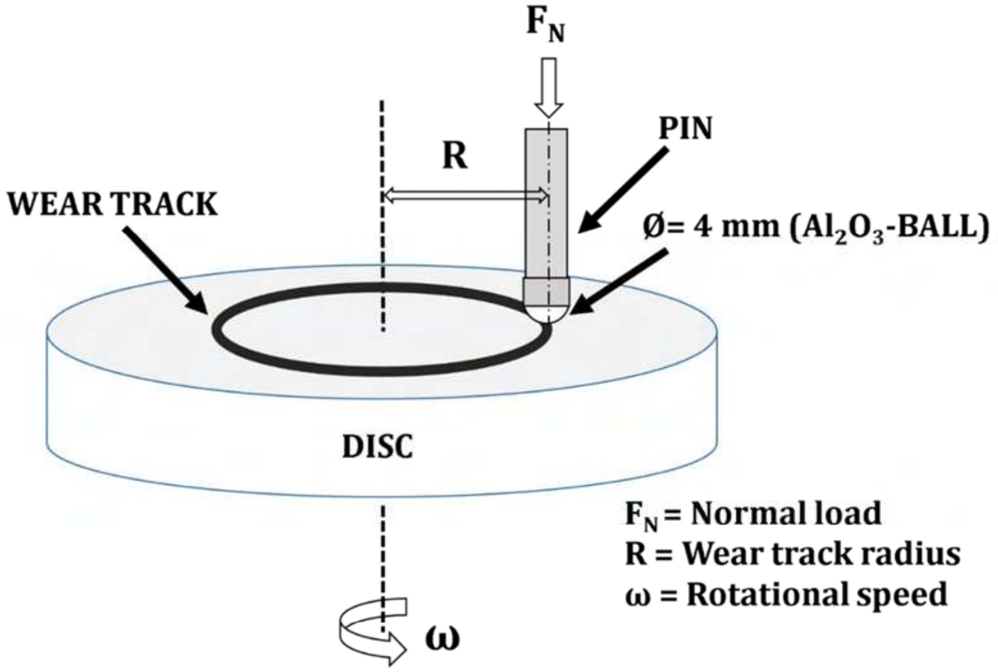

Fig. 2. Schematic of the ball-on-disc rotary configuration employed for the wear test.

2.5. Mechanical and chemical property characterization

The indentation prints created on the pristine surface after Vickers indentation were further analysed by optical microscopy (OM) and scanning electron microscopy (SEM). This was undertaken to characterize the indentation-induced deformation microstructure and crack deflection toughening of this MAX phase composite. The evolved chemistries at the sliding surface was probed by SEM-EDS elemental mapping in order to elucidate the evolution sequence of the tribofilms.

3. Results and Discussion

3.1. SPS sintering cycle

Fig. 3 shows the variation of temperature, applied force (pressure), punch displacement (piston movement) and sintering speed during the SPS cycle. As shown, the punch displacement has been divided into distinctive segments (I – IV) to represent the respective sintering stages and corresponding sintering events. In segment I, particle rearrangement initiated by the applied force resulted in positive punch displacement due to powder compression. A corresponding increase in sintering speed (~ 1.2 mm/min) due to the pistons moving together (compaction) is observed in segment I. In segment II, the densification stage, a slight positive piston displacement at a sintering speed ~ 0.3 mm/min in the temperature range 450-900 °C is observed. This is then followed by a sharp positive piston displacement from 900 °C up to the requisite sintering temperature 1350 °C at an increased sintering speed (~ 0.6 mm/min) owing necking and plastic deformation of the powder particles. In segment III, the requisite sintering temperature, the piston displacement is relatively constant at this stage as all the pores have been eliminated. The last segment (IV), the cooling stage, further positive piston displacement (~ 1.2 mm/min) due to thermal induced contraction is observed.

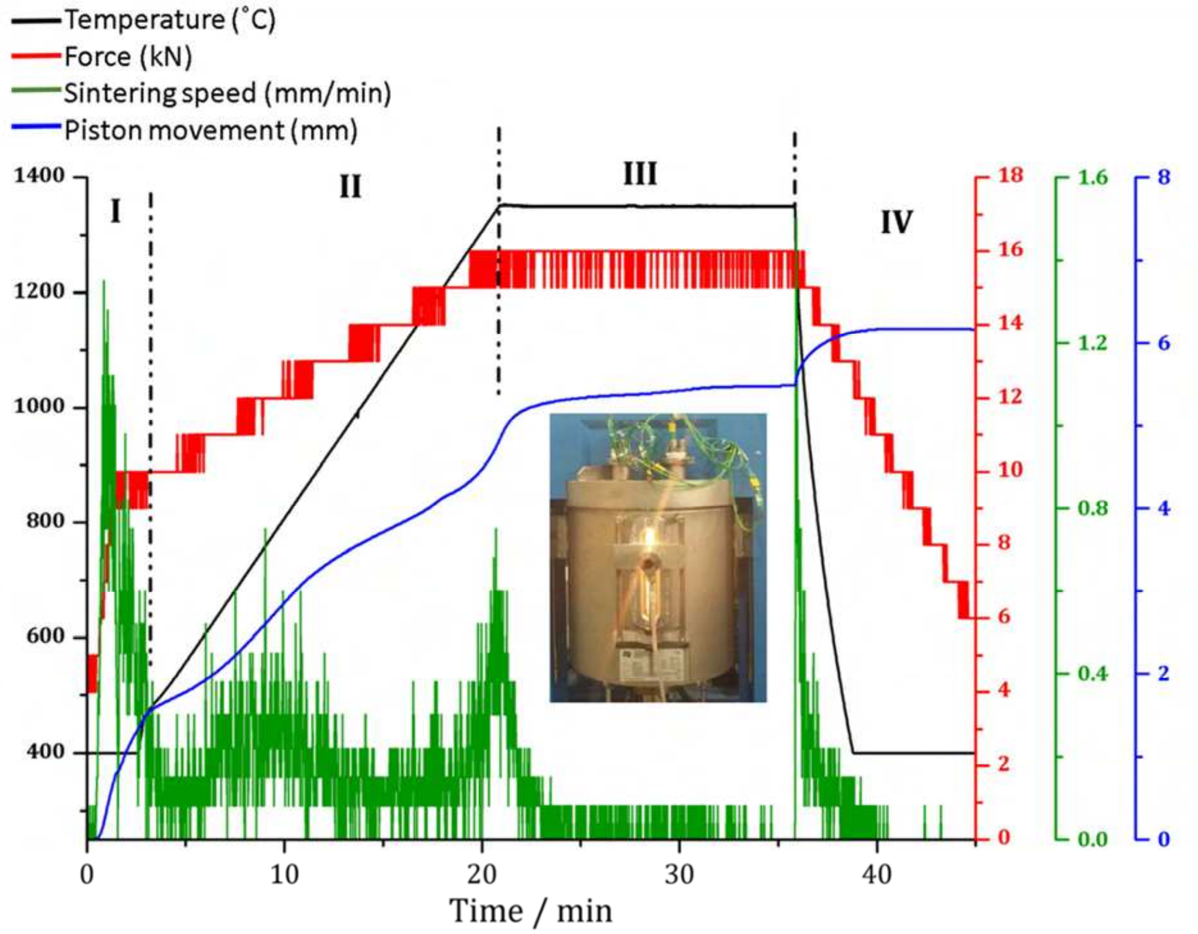

Fig. 3. SPS shrinkage profile during the synthesis of Ti_3SiC_2 metalloceramic under vacuum.

3.2. *Phase analysis and quantification*

The XRD phase identification of the polished disc is shown in Fig. 4. Ti_3SiC_2 is the main phase whilst TiC and $TiSi_2$ exist as the minor phases. The $TiSi_2$ ancillary phase is a compulsory intermediate phase leading to the formation of Ti_3SiC_2 [36]. The phase fractions as determined by Rietveld refinement (χ^2 2.504, R_p 0.0732, R_{wp} 0.0942) indicated 80 wt.% Ti_3SiC_2, 14 wt.% TiC and 6 wt.% $TiSi_2$, respectively.

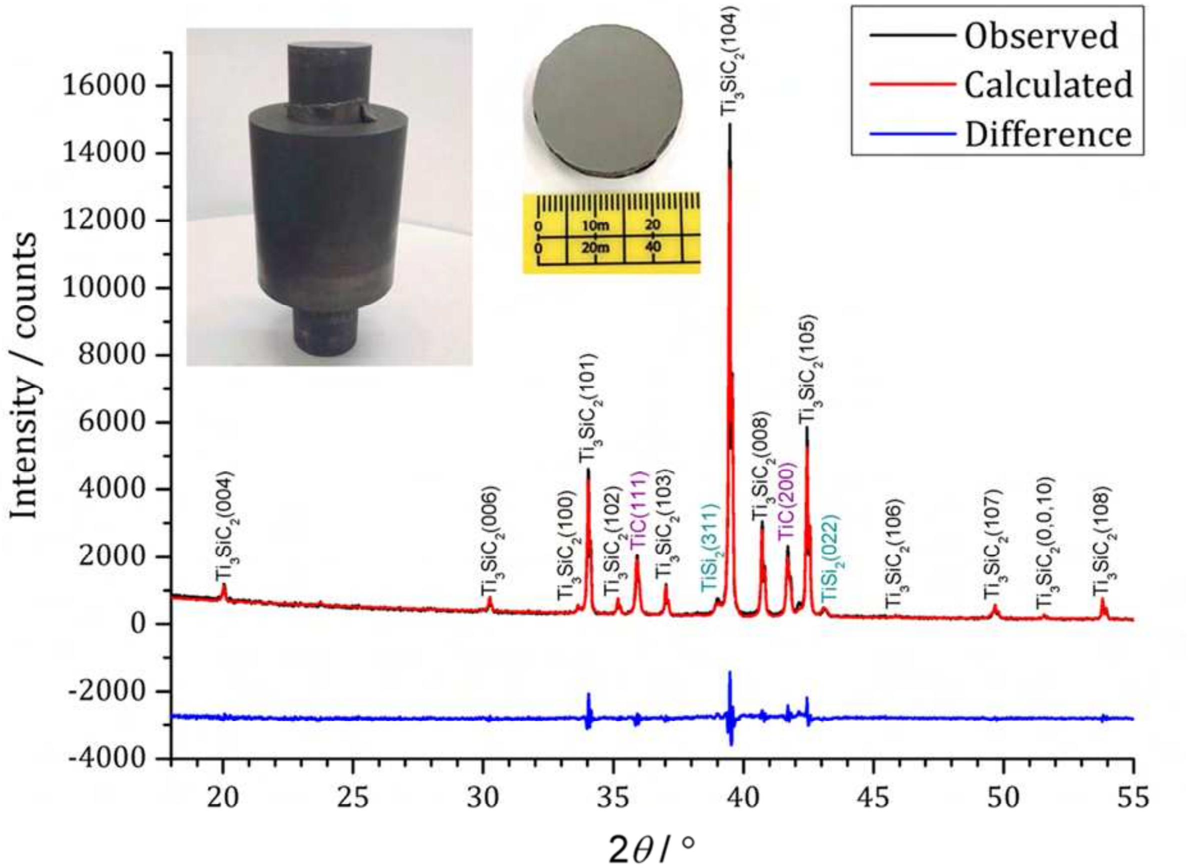

Fig. 4. XRD pattern obtained from the polished surface of the MAX phase composite disc. Inset shows the punch-powder-die set-up.

3.3. *Microstructural evolution*

A backscattered SEM micrograph obtained from the polished unetched SPSed disc surface is shown in Fig. 5. The bulk sample appears almost fully dense albeit some number of pores were observed. In agreement with XRD phase identification, EDS analysis (Fig. 6 and 7) showed the bulk sample contained the main phase Ti_3SiC_2 (bright contrast) as well as TiC (dark contrast) and $TiSi_2$ (medium contrast (red arrow)) as ancillary phases. According to Sato et al. [37], eutectic Ti-Si liquid forms around the eutectic temperature 1630 K; a compulsory intermediate phase from which Ti_3SiC_2 grows due to the coexistence of the eutectic liquid phase and TiC [38, 39] as follows [40]:

$$\mathrm{TiSi}_{2(s)} + 2\mathrm{TiC}_{(\mathrm{s})} \rightarrow \mathrm{Ti}_3\mathrm{SiC}_{2(\mathrm{s})} + \mathrm{Si}_{(\mathrm{g})}$$

The presence of Ti-Si liquid phase and TiC as ancillaries in the bulk sample may be attributed to incomplete synthesis reaction as the Ti-Si liquid phase has not been fully consumed during the synthesis [41]. It is noteworthy to mention that beside the incomplete reaction that might have led to the formation of ancillary phases, the reactions leading to the formation of Ti-Si and Ti_3SiC_2 are exothermic [42, 43]. This implies that the local temperature may have exceeded the melting point of Si (T_m =1414 °C), thus leading to possible Si evaporation. The loss of Si will cause a shift in the overall phase composition of the bulk sample to the Ti_3SiC_2–TiC–$TiSi_2$ three-phase region according to the Ti-Si-C equilibrium phase diagram [38, 44].

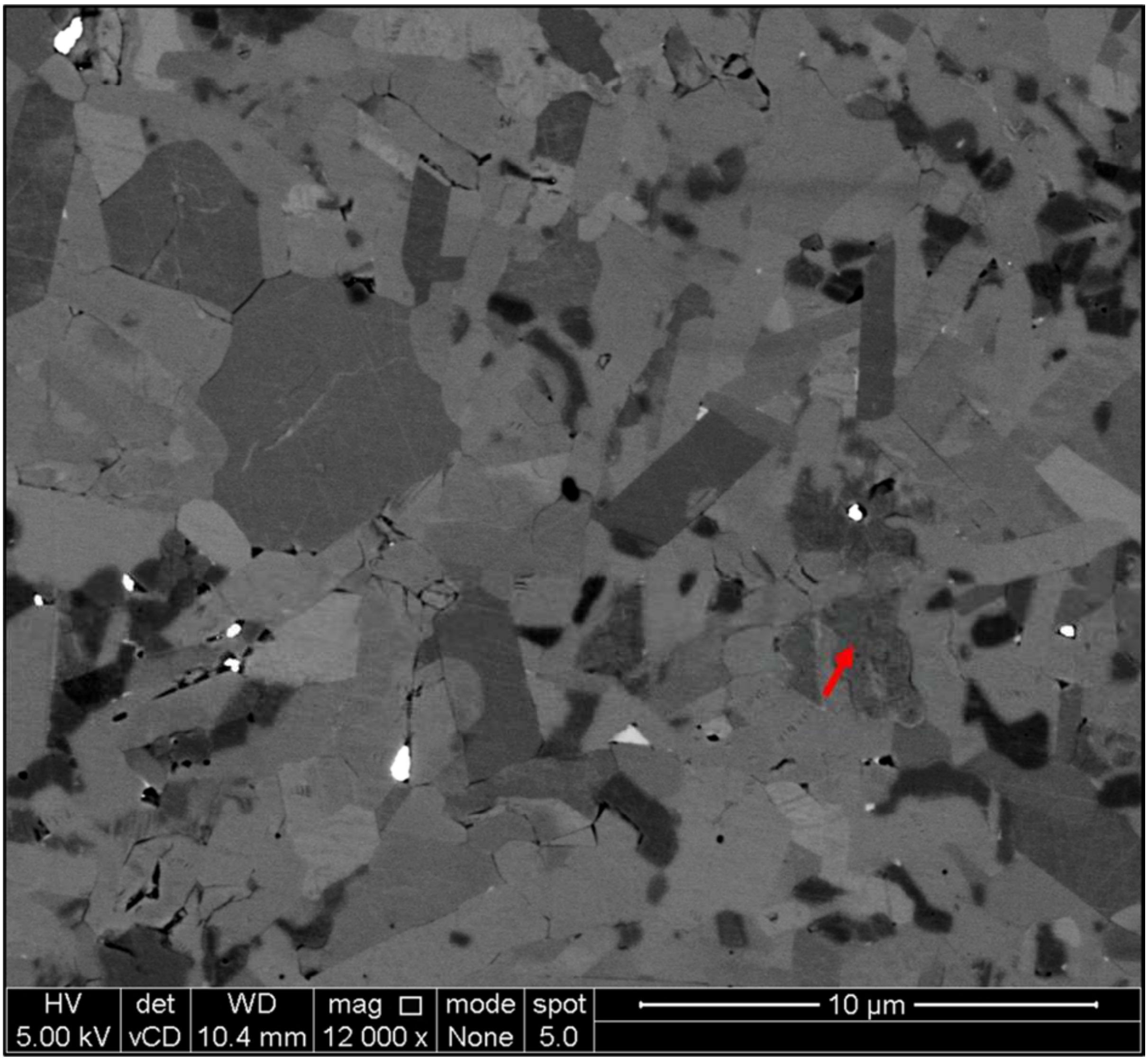

Fig. 5. A backscattered SEM micrograph of the unetched polished bulk sample. Note: white contrast are artefacts from colloidal silica used to reveal the microstructure without etching.

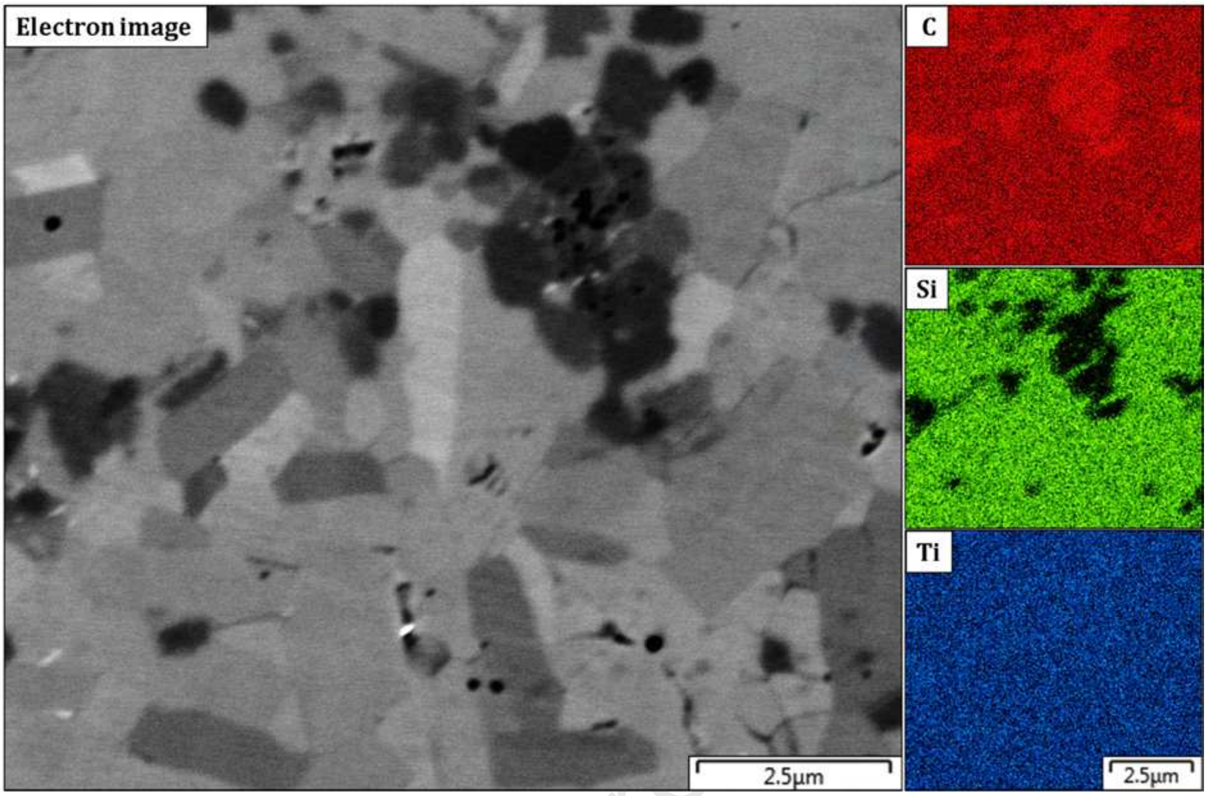

Fig. 6. EDS map showing the TiC regions (dark phase) in the bulk sample. TiC appears to form clusters in some region and moderately distributed in the Ti_3SiC_2 matrix.

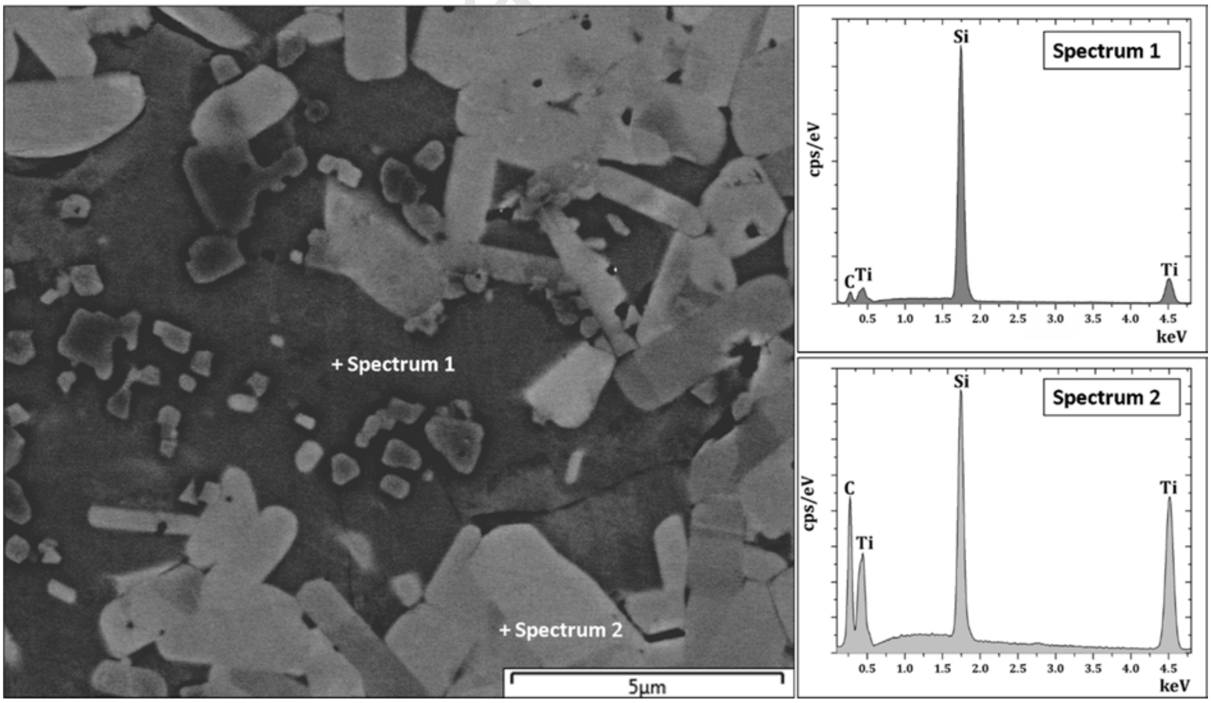

Fig. 7. EDS point spectrums showing the Ti-Si intermediate phase liquid region (spectrum 1) from which the growth of Ti_3SiC_2 (spectrum 2) occurred.

Fig. 8 shows typical transmission electron micrographs revealing the microstructural evolution of the pristine bulk sample. In agreement with the XRD phase analysis and SEM observation, the majority of the grains were Ti_3SiC_2 (Fig. 8(a)) with some TiC grains (white arrow) distributed in the Ti_3SiC_2 matrix as well as intergranularly (Fig. 8(d)). The in situ intergranular formation of TiC particles at the Ti_3SiC_2 grain boundaries is beneficial partly because it introduces a reinforcement at the TiC-Ti_3SiC_2 interface [33, 45]. The grain boundaries are the weakest point in the MAX phase matrix [31], as such, cracks easily nucleate at the grain boundaries, thus expediting grain pull-outs [33]. In addition, some few mobile dislocations (dash circle Fig. 8(c)) can be seen in the Ti_3SiC_2 grains; however, no other planar defects such as stacking faults were evident.

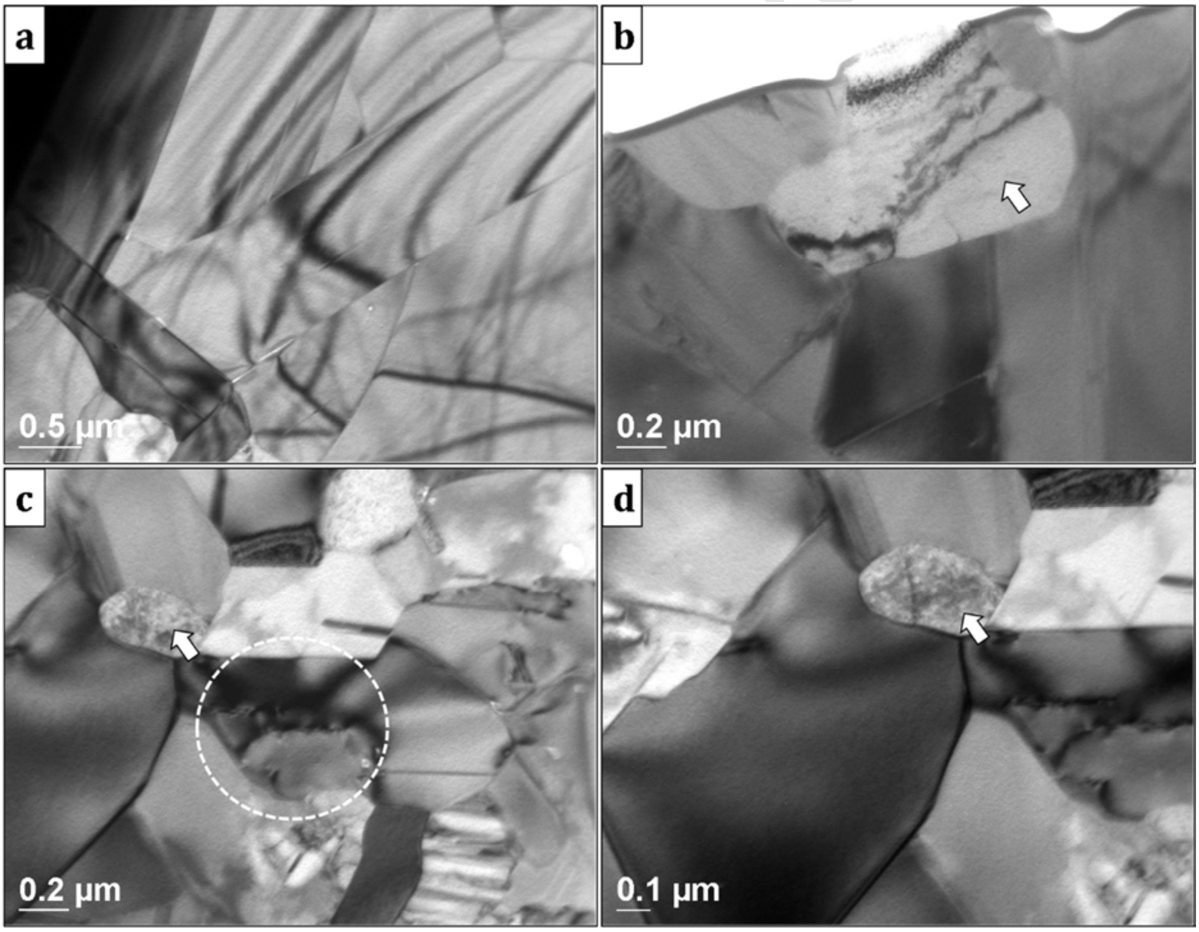

Fig. 8. Bright-field (BF) TEM micrographs showing microstructural evolution in the as-synthesized bulk sample. Fig. 8(d) is a higher magnification of Fig. 8(c) highlighting in situ intergranular formation of TiC particle (white arrow).

3.4. *Densification and hardness*

The relative density of the as-synthesized polished disc was ~ 98 % upon considering the phase fractions and theoretical densities of Ti_3SiC_2, TiC and $TiSi_2$ in the bulk sample using the mixture rule. Although some pores were seen in the as-synthesized disc as shown in Fig. 5, the bulk sample is nonetheless nearly fully dense. Vickers microhardness obtained from the polished surface of the disc was 7.8 ± 0.9 GPa. The measured bulk hardness is significantly higher than the reported theoretical hardness of monolithic Ti_3SiC_2 (~ 4 GPa) [46]. This increase can be ascribed solely to the TiC and $TiSi_2$ second phase particles in the bulk sample and is consistent with observations reported elsewhere [44, 45, 47].

Fig. 9 is an optical micrograph of the Vickers indentation prints and deformation pattern created using different indentation loads. An interesting feature from the observed deformed microstructure is the existence of extensive grain pile-ups and pull-outs around the indentation zones. These microscale plasticity events are examples of some of the typical energy absorbing deformation modes observed in MAX phases [46] contributing to their signature damage tolerance property [4, 48]. Furthermore, no radial cracks were seen at the indent diagonals, except for ring cracks around the indents. Such annular ring cracks suggest plastic deformation might be enabled by shear sliding in the bulk sample as reported elsewhere [49]. It is noteworthy to mention that the extent of grain pile-ups and grain push-outs around the indents were different for the same indentation load (Fig. 9) at different points. This asymmetry in the damage zones around the indents for the same indentation load is linked to the anisotropic behaviour of Ti_3SiC_2 [13]. During Vickers indentation, favourably oriented grains parallel to the surface are easily pushed out in the vicinity of the indentation towards the surface as they are relieved of compressive stresses [13, 46].

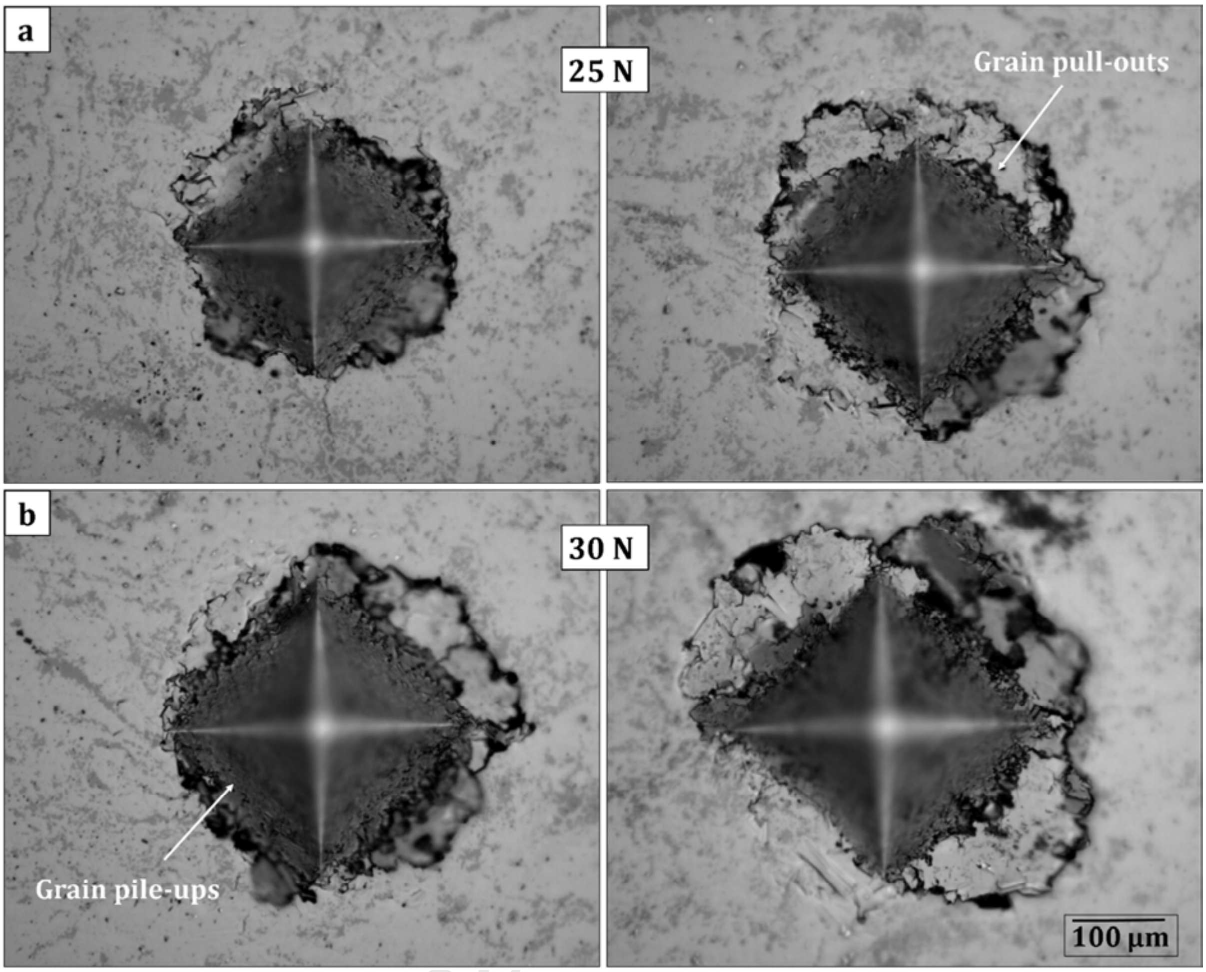

Fig. 9. Optical micrographs taken from the indentation damage prints made by (a) 25 N and (b) 30 N indentation loads, respectively.

Further, some other microscale plasticity events around the indentation damage zone not visible by optical microscopy were observed using scanning electron microscopy. Secondary electron (SE) micrographs (Fig. 10) shows a range of damage mechanisms such as grain pile-ups (Fig. 10(b)), grain delamination and buckling (black arrow), kink band (KB) formation (red arrow), and eventual cavitation (Fig. 10(e)). The nature of the damage in the neighbourhood of the indentation indicates that Ti_3SiC_2 exhibits microscale plasticity at room temperature [13] albeit lacking the five independent slip systems required for ductility [50], thus the observed cavitation.

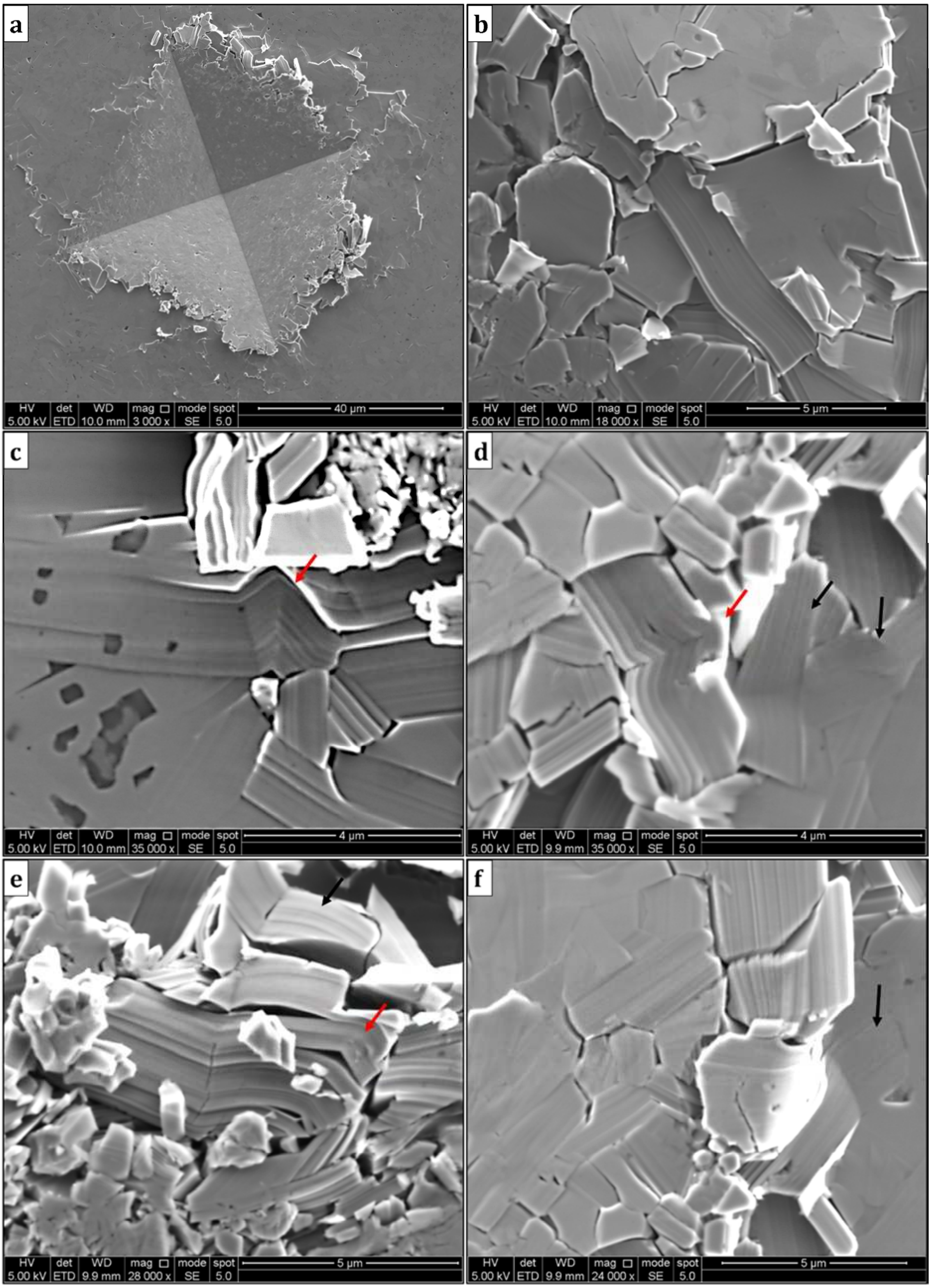

Fig. 10. SEM micrographs revealing the damage micromechanisms around the neighbourhood of the indentation prints created in the Ti_3SiC_2 – $TiSi_2$ – TiC composite. Note: In Fig.10(e) cavities are seen to have opened up between layers after extensive kink band formation.

Fig. 11 shows the morphology of crack propagation within the fractured section contained in the indentation zone (Fig. 10). A propagating crack was deflected extensively as it met an elongated Ti_3SiC_2 grains. Taking into account the microscale deformation mechanisms around the indentation, as well as the energy consuming crack propagation path within the damage zone, these observations reinforce the conclusion that the Ti_3SiC_2-$TiSi_2$-TiC composite is damage tolerant.

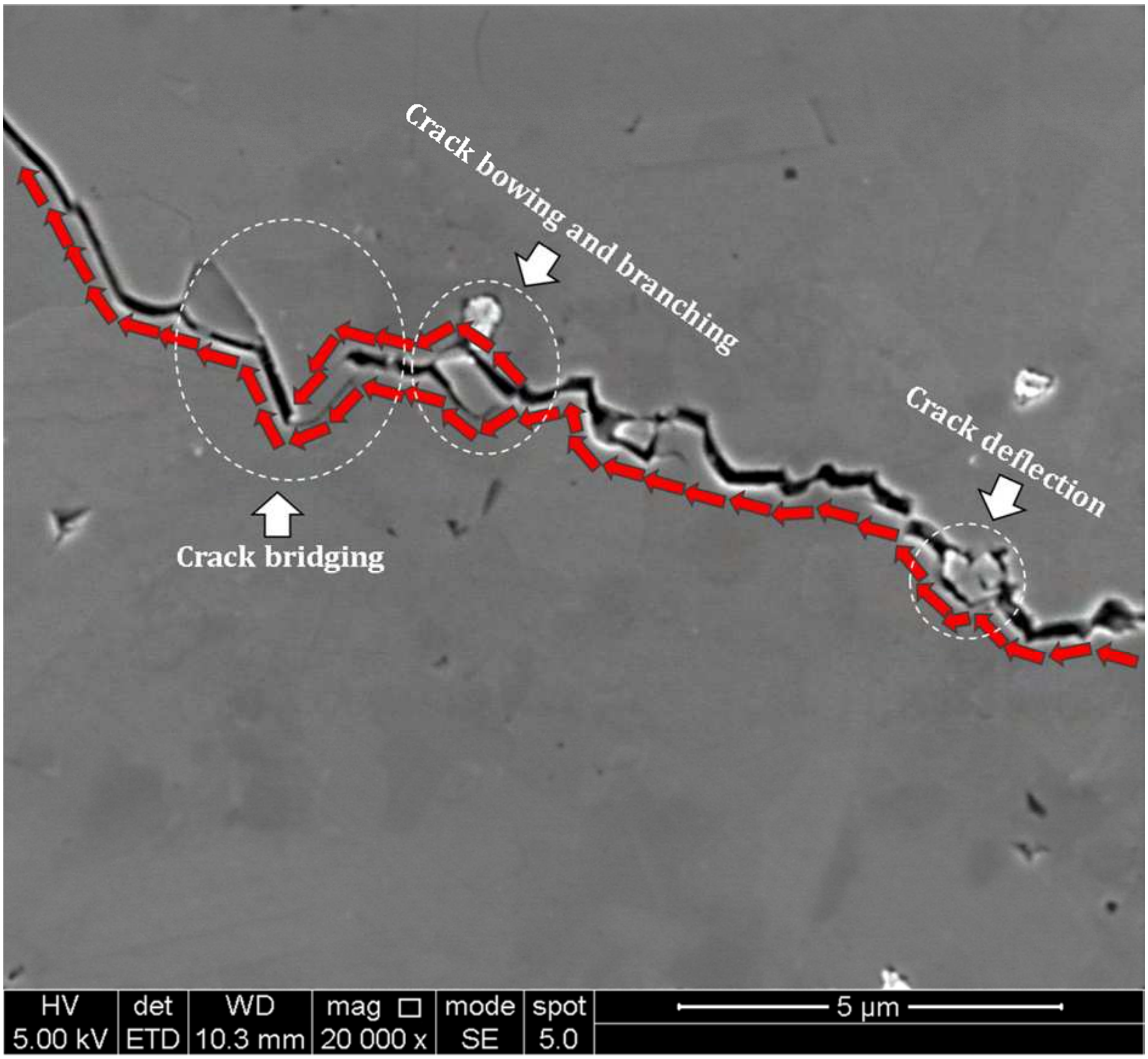

Fig. 11. Secondary electron (SE) SEM micrograph revealing the energy consuming crack propagation path in this composite system.

4. Tribological behaviour

4.1. Friction and wear

The evolution of friction coefficient as a function of time for the contact condition [0.5 N/50 rpm/60 min] and [0.5 N/100 rpm/ 30 min] are shown in Fig. 12. The noticeable features of these plots are the friction transition(s) and mild stick-slip phenomenon. The friction plots have been divided into three regimes (I, II, and III). In regime I, the friction was initially very low with no visible wear scar. This was then followed by a transition in friction to a high friction regime II, where the wear scar became visible. For the test condition [0.5 N/50 rpm/60 min], a later transition from high friction (regime II) to a low friction (regime III) is further observed. The transition in friction is consistent with observations reported elsewhere [27, 30]. The reason for the transition in friction and wear is not fully understood, however, it may be linked to a possible tribofilm formation and/or spallation taking place at the sliding surface. The stick slip event, on the other hand, may be attributed to possible adhesion between the ball and disc at the friction transition point due to the transfer of oxidized wear debris and/or spalled tribofilm to the ball. The wear rate for the entire test cycles were (0.74 ± 0.20)x10^{-4} $mm^3N^{-1}m^{-1}$ for the test condition [0.5 N/50 rpm/60 min] and (0.15 ± 0.35)x10^{-3} $mm^3N^{-1}m^{-1}$ for the test condition [0.5 N/100 rpm/30 min], respectively. Several attempts were made to measure the wear rate of the disc in regime I, however, the wear track could not be measured using the conventional stylus profiler. Analysis of the disc surface prior to friction transition (regime I) by SEM indicated that the polished surface had remained relatively unchanged. This is possibly because the tribolayer observed at the sliding surface prevented the ball-to-disc contact in this regime leaving the sliding surface relatively undamaged.

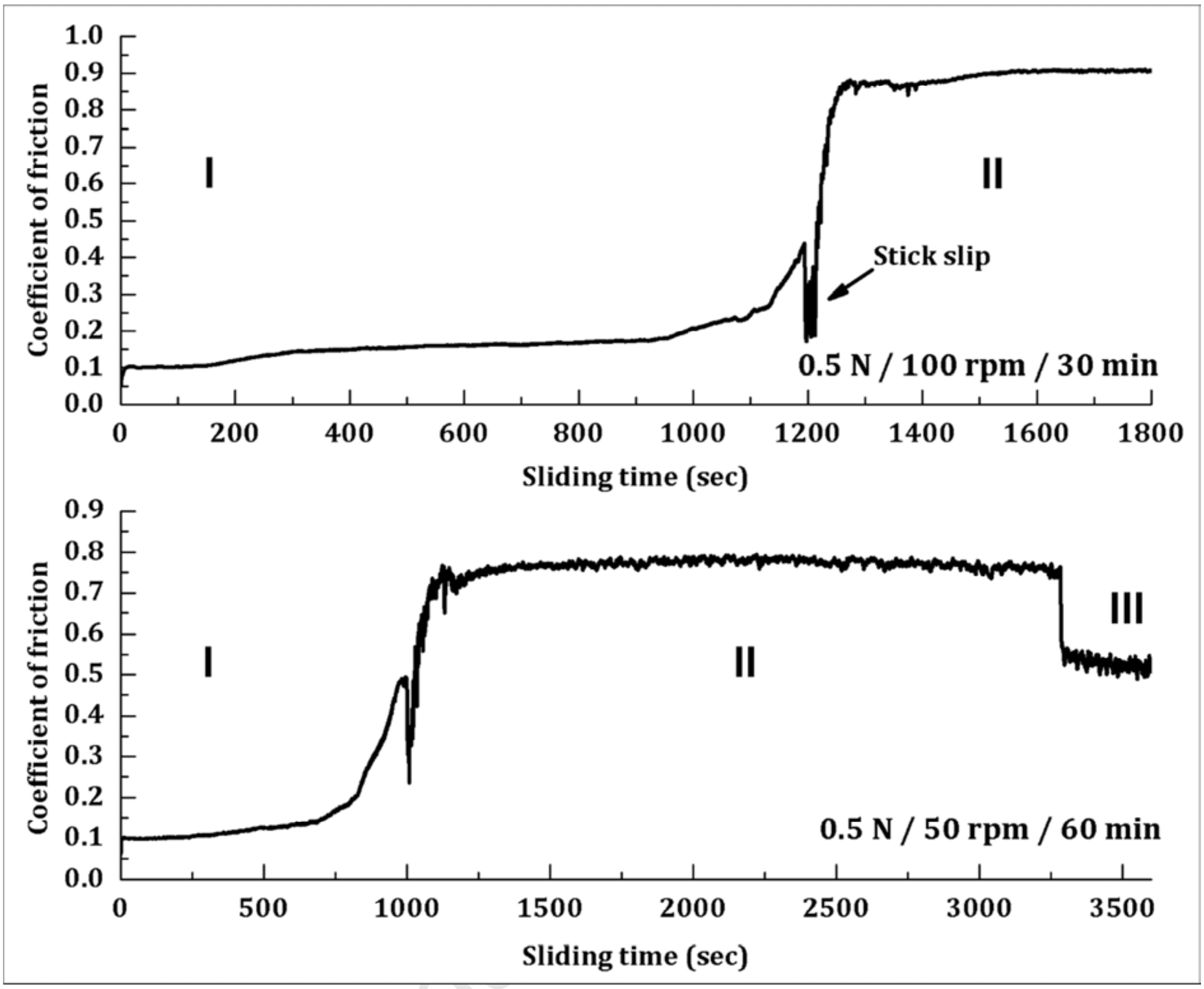

Fig. 12. Evolution of the friction coefficients as a function of sliding time for the test conditions.

4.2. Worn surface analyses

The worn surface from the test conducted at 50 rpm for 60 min was characterized preferentially for evidence of intrinsic lubricity and underlying wear mechanism in the following sections since it exhibited 3 distinct wear regimes (I-III).

4.2.1 Scanning and transmission electron microscopy characterization

SEM micrographs of the deformed microstructure obtained from the worn surface are shown in Fig. 13. Tribofilm formation (Fig. 13(a)) as well as tribofilm mixed with oxidized wear debris (Fig. 13(b)) were evident at the sliding surface. In agreement with the deformation microstructures upon Vickers indentation, grain delamination and kink band formation were also observed from the SEM micrographs of the worn disc surface. A cavity created upon grain pull-outs (Fig. 13(e)) served as a wear debris reservoir for the pulverized fractured grains (Fig. 13(f)).

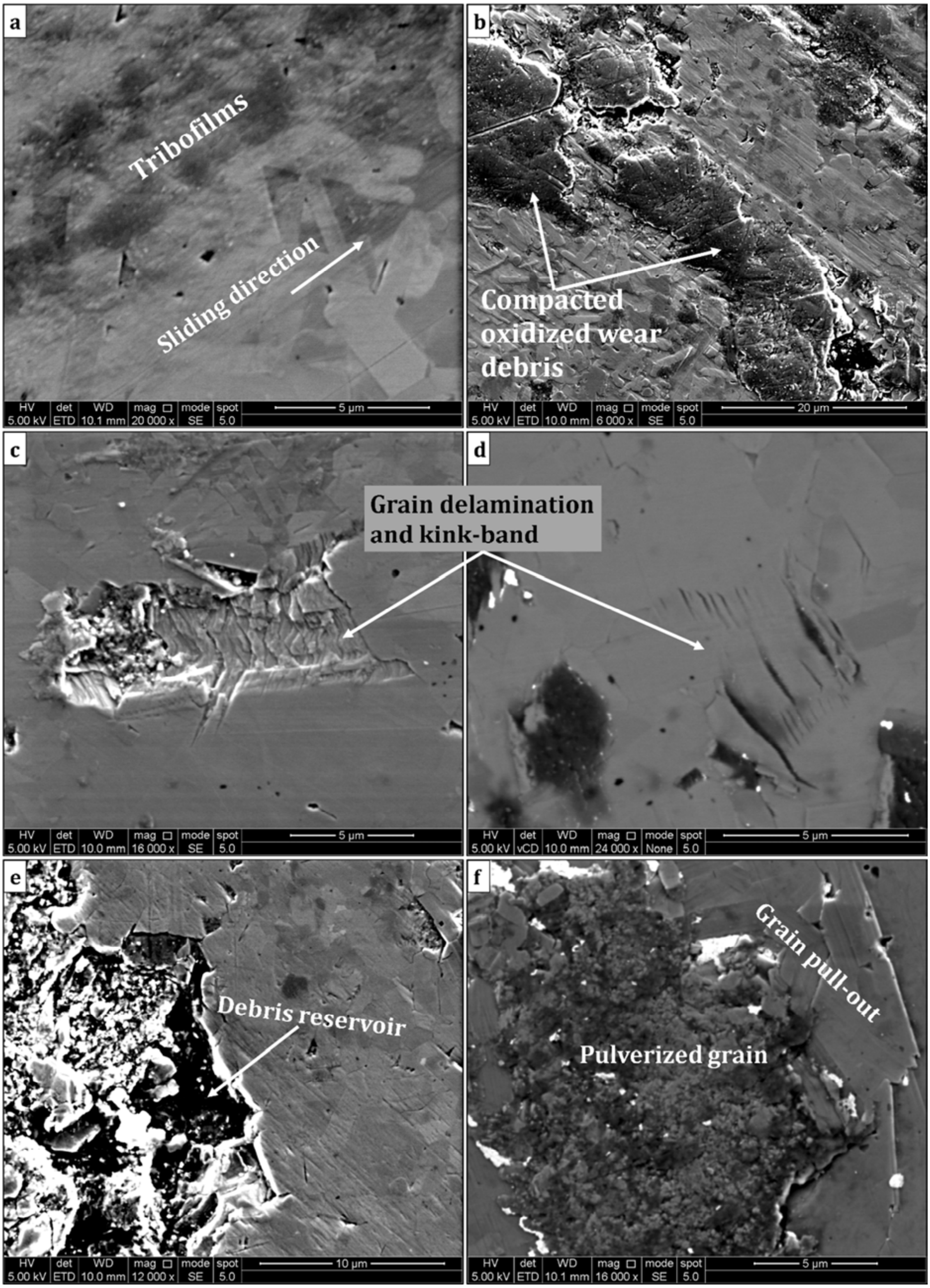

Fig. 13. Secondary electron (SE) SEM micrographs obtained from the worn surface of the disc.

Fig. 14 shows the cross-sectional bright-field (BF) STEM electron image obtained from inside the wear track alongside with associated EDS map analysis employed to identify the phases. The plate-like grains are all Ti_3SiC_2 grains whilst the equiaxed-like grains are the TiC grains.

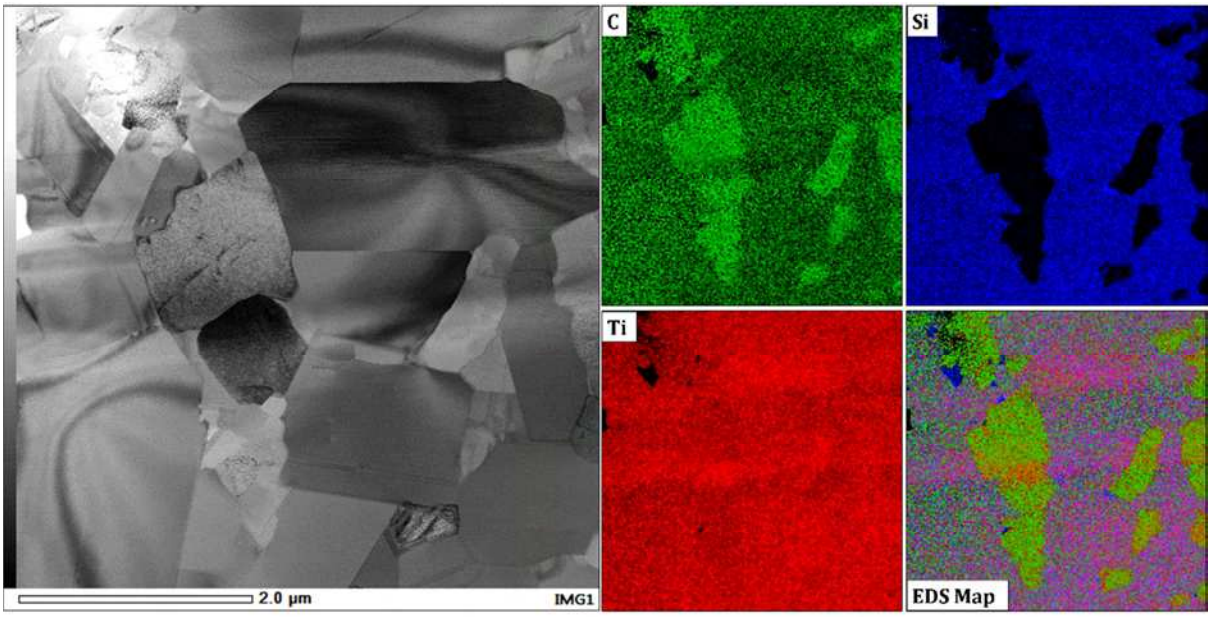

Fig. 14. STEM/EDS chemical mapping of the cross-sectional FIBed section from the worn surface.

A collection of TEM images from the worn surface of the Ti_3SiC_2-$TiSi_2$-TiC composite revealing various shear-induced deformation microstructures are presented in Figs. (15-18). Extensive stacking faults (SFs) running parallel across the Ti_3SiC_2 grains is shown in Fig. 15. The absence of stacking faults in as-SPSed bulk sample supports the reasoning that they are not linked to stacking errors in the layer sequence i.e., the lack of an A-layer and/or insertion of an MX-layer during the SPS synthesis. The stacking faults appears to be a planar defect initiated during the sliding contact in agreement with observation reported elsewhere [3]. According to Barsoum et al. [51], the deformation leading to kink band formation will cause the re-orientation of the basal plane in the kinked region, thus bringing about lattice rotation. This lattice distortion due to kink band (KB) formation possibly led to missing atomic planes and consequently leading to stacking faults in the worn sample. Fig. 15(e) is a bright field STEM image of the deformed Ti_3SiC_2 grain and the corresponding SAED patterns. Corresponding HRTEM image of Fig. 15(e) shows basal plane stacking faults induced by the distortion of the lattice structure and are marked as white arrow in Fig. 15(f).

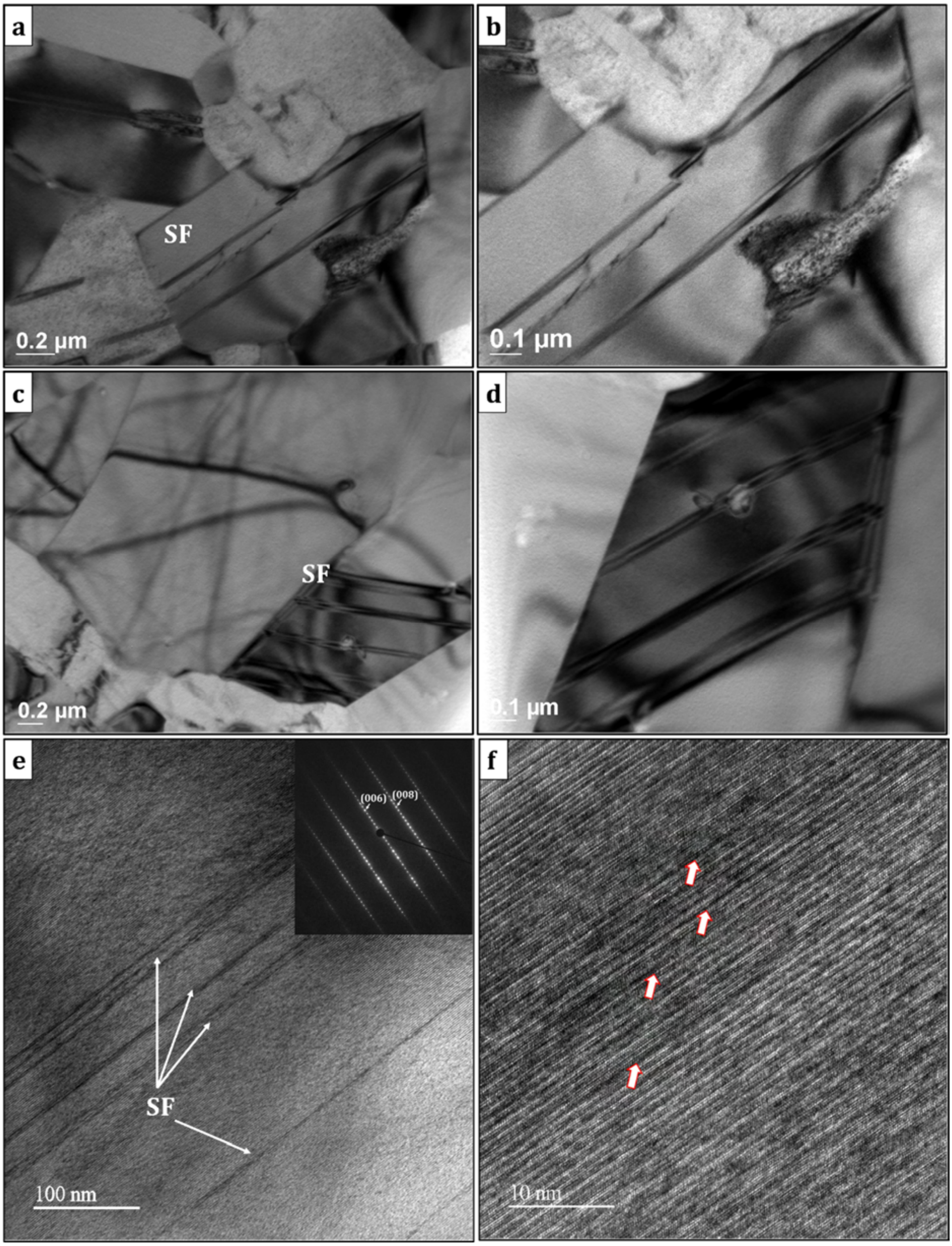

Fig. 15. Bright-field (BF) TEM micrographs showing extensive stacking fault (SF) propagation across the Ti_3SiC_2 grains: (b) is a higher magnification of (a), (d) is a higher magnification of (c), (e) bright-field (STEM) revealing stacking faults across a Ti_3SiC_2 grain with inset showing corresponding SAED pattern and (f) HRTEM image taken from the Ti_3SiC_2 grain.

Fig. 16 shows a range of mechanisms leading to eventual crack formation in the Ti_3SiC_2 matrix. The deformation of the Ti_3SiC_2 matrix as the resolved shear stress exceeds a critical value during sliding contact will result in Ti_3SiC_2 grains shearing away relative to each other. As a consequence, there will be crack formation at the grain boundary such as those observed in Fig. 16 (a and b) [52]. Fig. 16(c) shows an open crack formed owing to continuous shear stresses that have led to the separation of dislocation walls, thus the evolution of kink bands (KBs) in consistent with observations elsewhere [52]. It is not surprising that wear induced deformation of Ti_3SiC_2 led to cavity formation (Fig. 16(c)) as this is consistent with indentation-induced cavitation (Fig. 10(e)) seen around the Vickers indentation prints. Some cracks propagating across the grains such at that shown in Figure 16(d) were also observed.

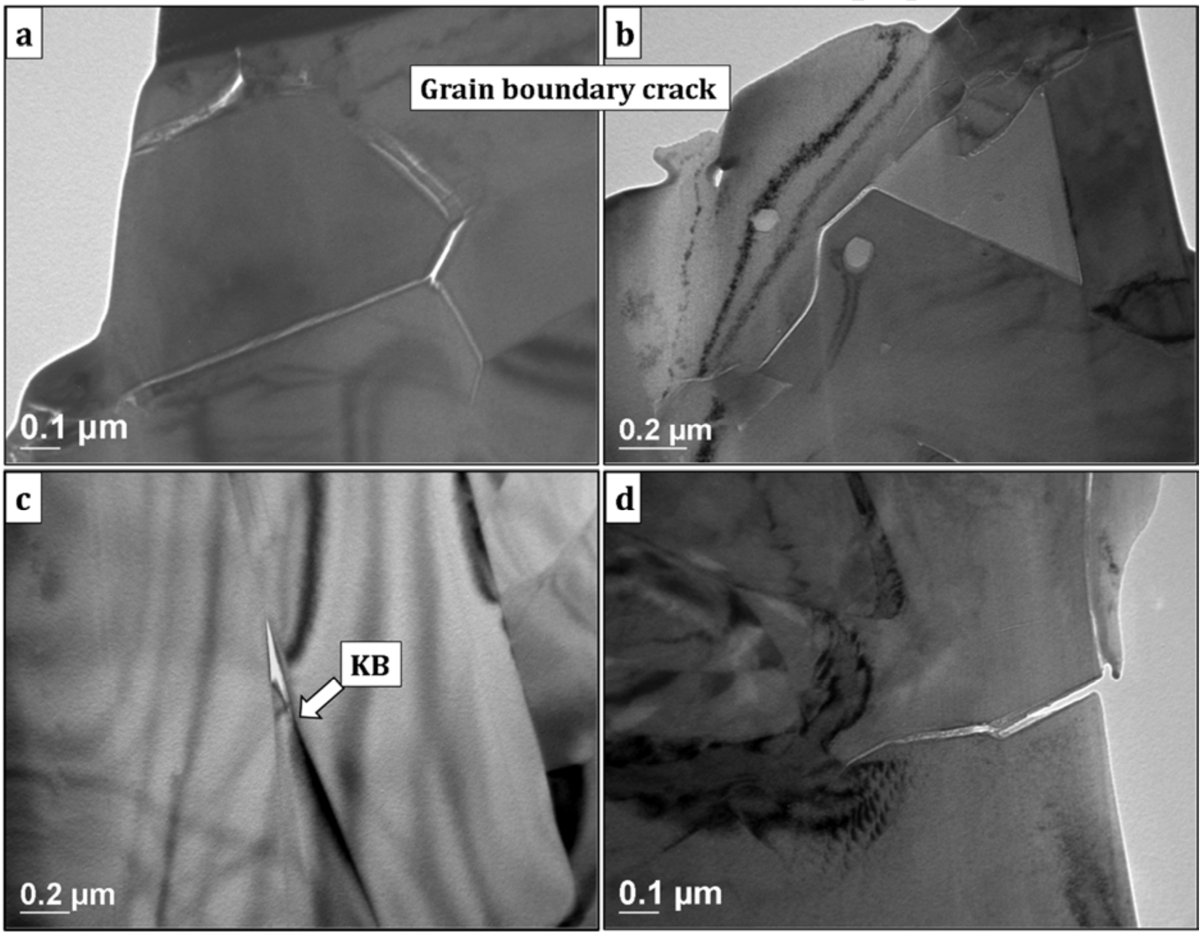

Fig. 16. Bright-field (BF) TEM images showing (a-b) grain boundary cracks, (c) kink band (KB) containing crack along the kink boundary and (d) crack propagating across the Ti_3SiC_2 grain.

Fig. 17 is bright-field TEM micrograph of an area where both the Ti_3SiC_2 and TiC phases coexist in the worn section. As shown, defect clusters in the form of dislocation debris are evident in some of the TiC grains (white arrow) and indicates the deformation of TiC phase during the sliding action. It appears the TiC particles shielded the Ti_3SiC_2 matrix by acting as the load-bearing elements. In addition, the TiC particles tends to reinforce the grain boundary in areas where TiC formed intergranularly as no cracks were observed in these worn regions (Fig. 17 (e and f)) in contrast to grain boundary regions where TiC particles are absent such as in Fig. 16 (a and b).

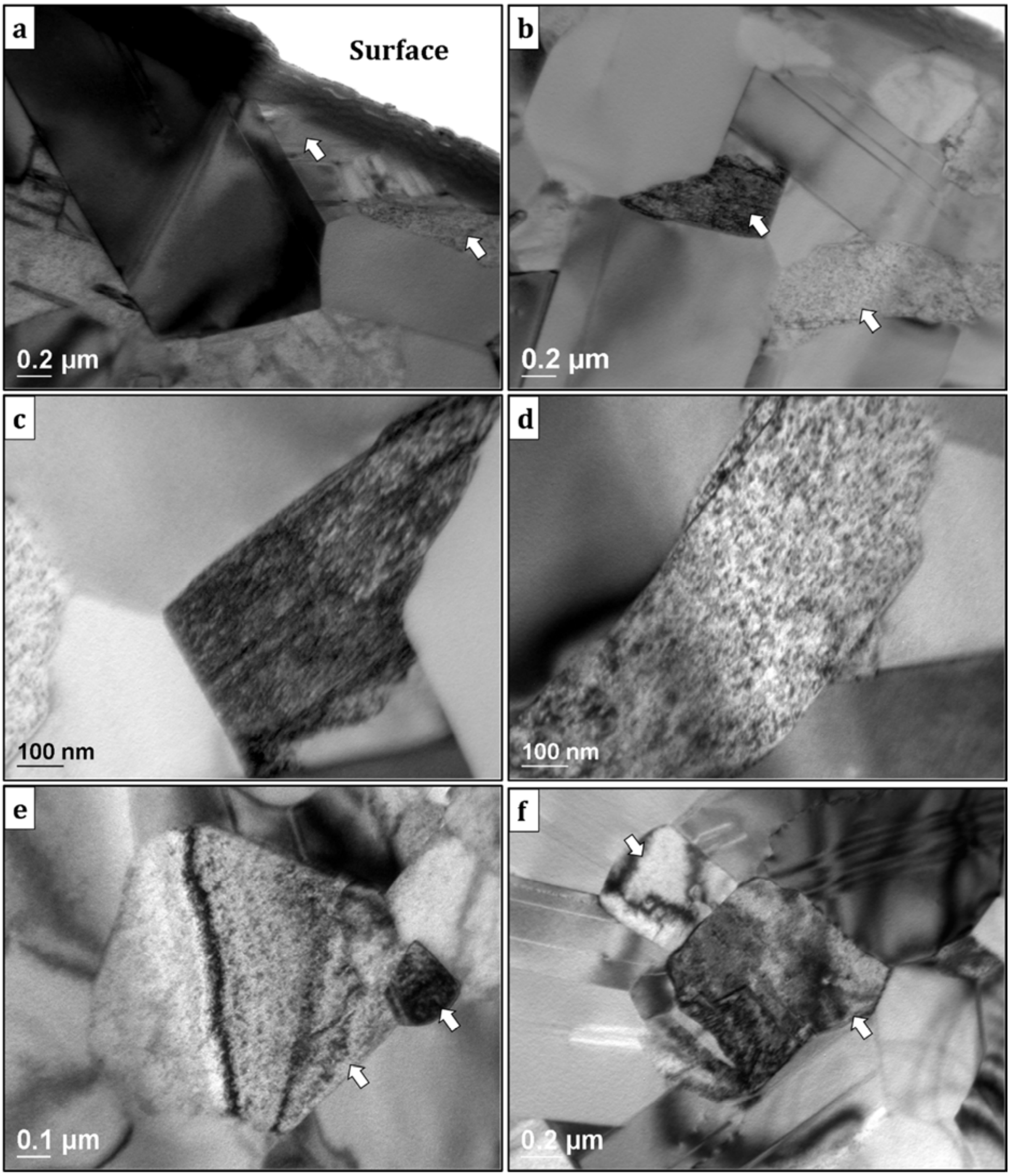

Fig. 17. Bright-field TEM micrographs of the worn surface of the composite showing: (a and b) load-bearing TiC particles (white arrow), (c and d) higher magnification of the TiC particles (white arrows)

in (b), and (e and f) shows the absence of grain boundary fracture at the Ti_3SiC_2/TiC deformed grain boundary.

Fig. 18(a) shows the evolution of dislocation walls across the Ti_3SiC_2 grain. The formation and eventual separation of dislocation walls due to shear stresses has been linked to delamination cracks in Ti_3SiC_2 [52, 53]. High dislocation density due to dislocation pile-ups can be seen in the Ti_3SiC_2 grain (Fig. 18 (b)), indicating stress concentration prior to grain fracture. It is conceivable that, the observed crack propagation across the Ti_3SiC_2 grains (Fig. 16(d)) is as a result of stress nucleation, concentration and eventual crack formation.

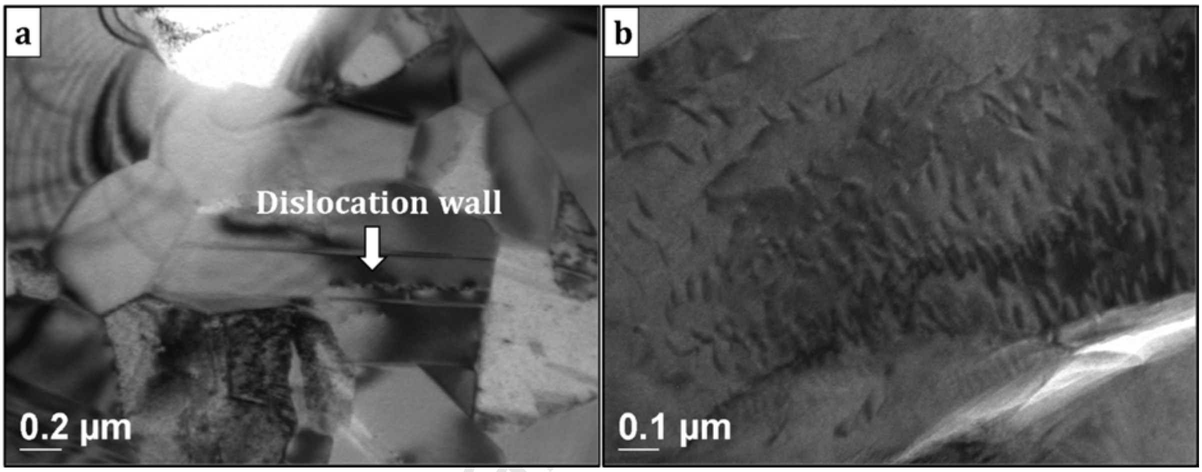

Fig. 18. Bright-field TEM images showing the evolution of: (a) dislocation wall and (b) dislocation multiplication in the Ti_3SiC_2 grains.

4.2.2. *Raman and EDS analyses*

Raman spectrum collected from the pristine sample (Fig. 19) displayed peaks corresponding to Raman vibrational modes of Ti_3SiC_2 [54-56] and $TiSi_2$ [57], respectively. It is worthy to mention that TiC peaks were not detected as stoichiometric TiC does not possess Raman-active vibrational modes [54]. Also, the absence of non-stoichiometric TiC_X which possesses Raman active vibrational modes supports the fact that; Ti_3SiC_2 neither decompose at the SPSed requisite sintering temperature (1400 °C) due to Si evaporation nor the possible carbon diffusion from the graphite tooling and subsequent reaction with Ti_3SiC_2 (i.e., carburization) that might have led to TiC_X formation as follows [58]:

$$\mathrm{Ti_3SiC_2 \rightarrow 3TiC_{0.67}(s) + Si(\uparrow)} \qquad (1)$$

$$\mathrm{Ti_3SiC_2 + (3x - 2)C = 3TiC_x\ (x > 0.8) + Si} \qquad (2)$$

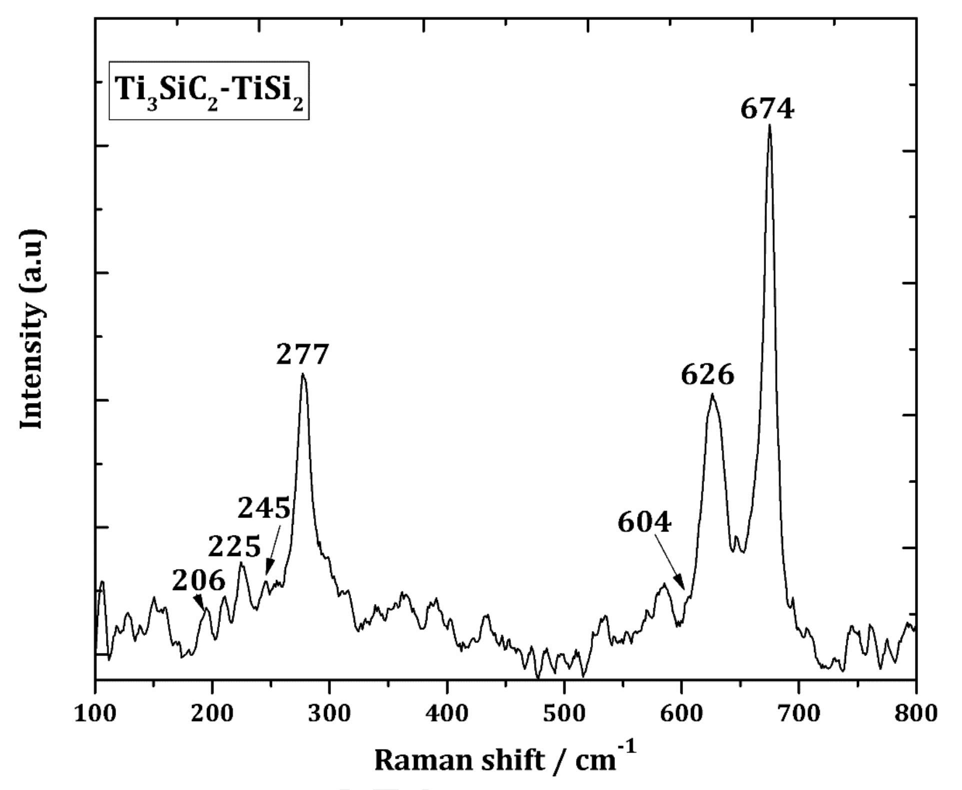

Fig. 19. Raman spectrum collected from the pristine surface of the Ti_3SiC_2–$TiSi_2$–TiC composite. Peaks at 206 cm^{-1} and 245 cm^{-1} corresponds silicide vibrational modes.

Raman spectra were further collected from the pre and post-transition worn surface (Fig. 20) in order to elucidate the transition in friction. Raman spectrum collected from the pre-transition worn surface containing an iridescent tribofilm displayed the presence of evolved graphitic carbon at the sliding surface. On the other hand, the post transition worn surface chemistry showed that in addition to the graphitic carbon evolved at pre-transition worn surface, anatase (TiO_2) and titanium oxycarbide (TiC_XO_Y) later evolved at the post-transition sliding surface.

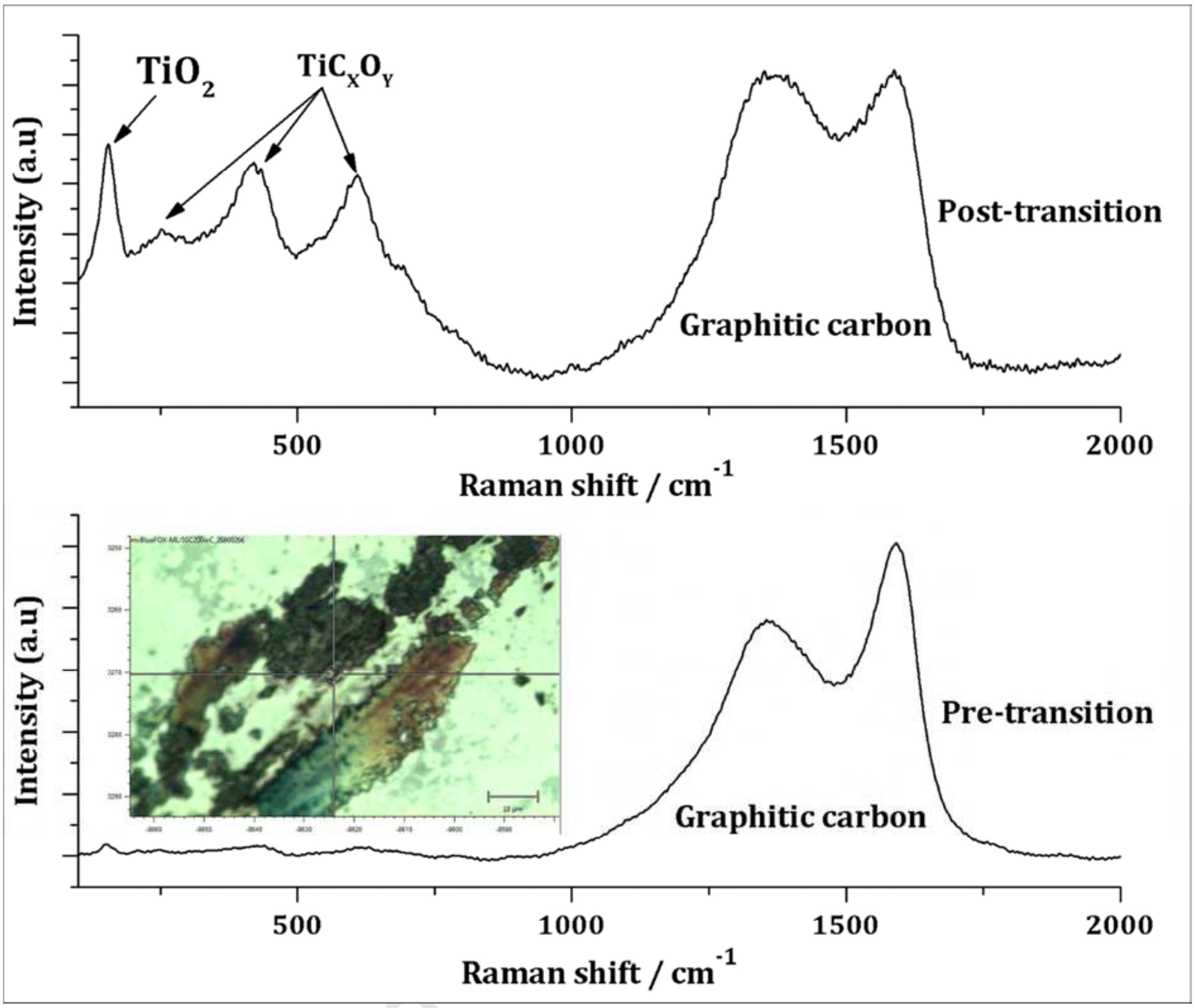

Fig. 20. Raman spectra collected from the pre and post-transition worn surfaces of the disc. In set shows iridescent tribofilm at the pre-transition sliding surface.

SEM-EDS analysis undertaken to further probe local changes in chemical structure of the wear track is presented in Fig. 21. Oxidation of the worn surface was evident in agreement with Raman analysis. The EDS map further showed depletion of carbon in the oxidized region whilst the Ti and Si-regions were heavily oxidized. A pool of graphite rich material was seen within the wear track which is again consistent with the Raman analysis pre-transition (Fig. 20) which revealed evidence of graphitization. This wear-induced oxidation can be linked to the flash temperature developed at the asperity contact as well as frictional heating due to the dry sliding condition. Further, evidence of material transfer (Al onto the sliding surface) was seen in the wear track and signifies possible localized adhesive wear. The adhesion between the ball and disc may be responsible for the stick slip events observed at the transition point.

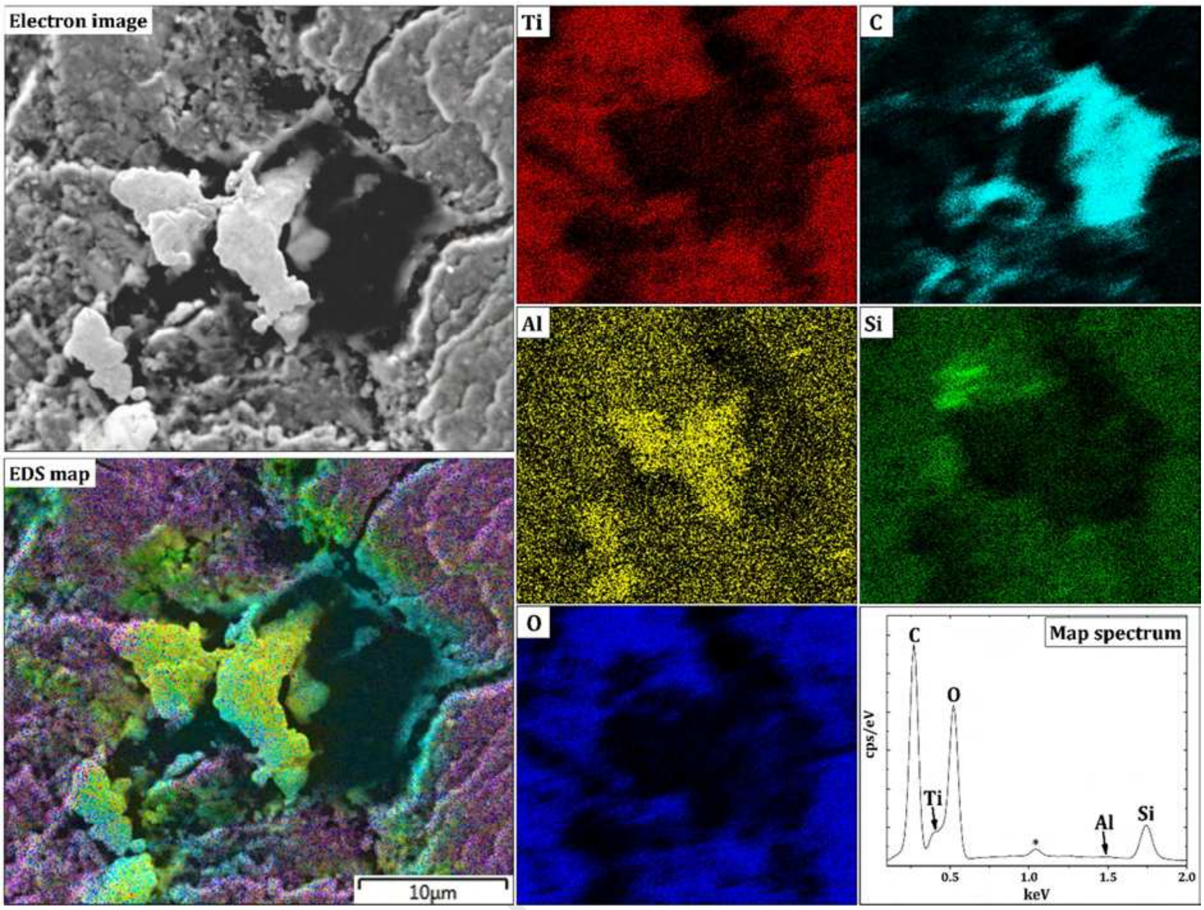

Fig. 21. SEM-EDS chemical map and spectrum taken from inside the wear track of Ti_3SiC_2–$TiSi_2$–TiC/Al_2O_3 tribo-pair for the test condition at 50 rpm.

4.3. *Friction transition surface evolution and ball analysis*

Fig. 22 shows the evolution of surface microstructures corresponding to regime I – III from the friction plot of the test conducted at 50 rpm for an hour. As shown in Fig. 22(a), in regime (I) a very thin layer of graphitic tribofilm evolved across at the sliding surface, preventing ball-to-disc contact, as such, the sliding surface was largely undamaged. Regime (II) revealed extensive damage at the sliding surface due to the tribofilms being worn off. The depletion of tribofilm at the sliding surface consequently led to contact between the tribocouple in regime II. In addition, cavities left behind as a result of grain pull-outs upon ball-to-disc contact act as reservoirs for wear debris as highlighted in Fig. 13(e). In regime III, surface smoothing and/or surface healing due to repeated sliding can be seen. This helped create a smooth surface for stable re-graphitization. Fig. 22(b) further highlights the details of the tribofilm architecture leading to friction transition from regime I – II. As shown, smearing of tribofilms along the sliding surface took place as the anatase and oxycarbide tribofilms evolved. The smeared layer is then spalled off over time leading to the eventual ball-to-disc contact, thus the generation of abrasive wear debris.

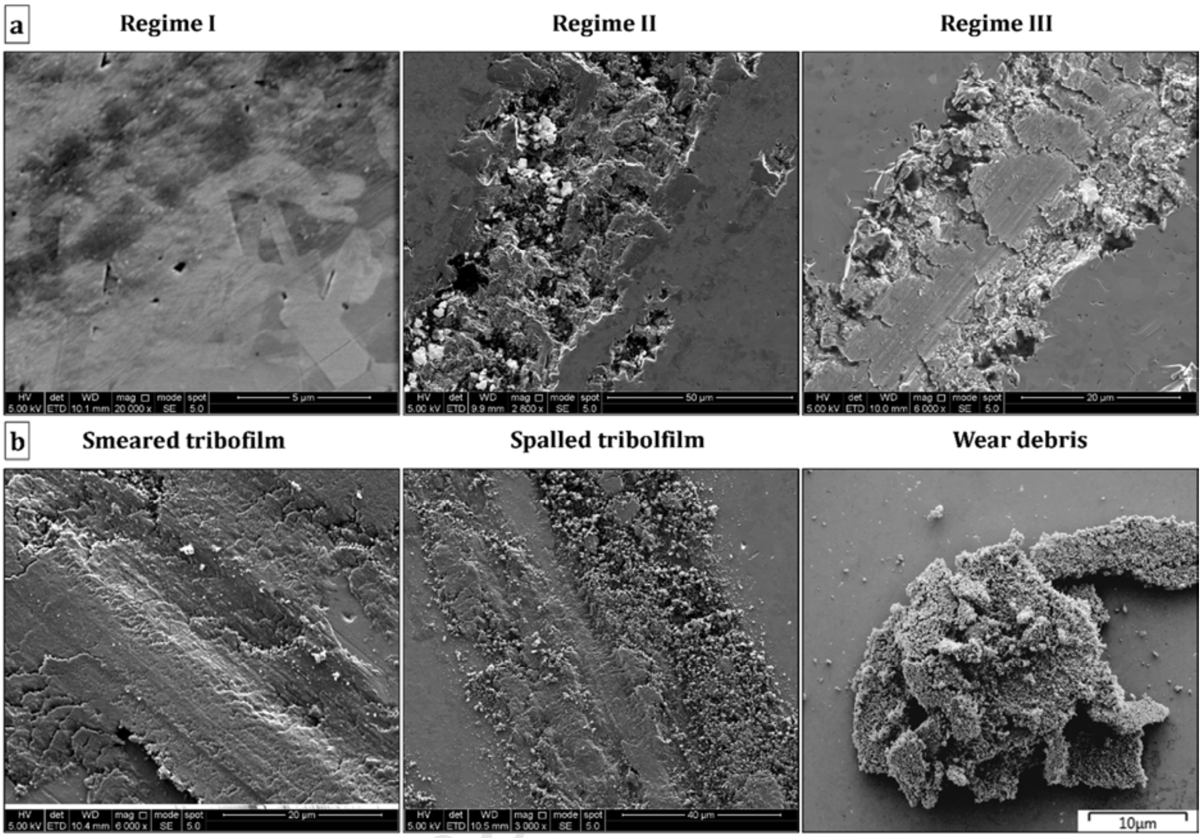

Fig. 22. (a) evolution of surface microstructures corresponding to regimes I – III, and (b) details of surface microstructure leading to transition from regime I – II as observed in the friction plot for the test conducted at 50 rpm.

The morphology of the Al_2O_3 ball was observed at the end of the sliding time (that is, test conducted at 50 rpm for 60 min) using an optical microscope and a surface profiler. Evidence of transfer film from the disc to the ball surface is shown in Fig. 23(a). In addition, mild wear grooves (Fig. 23(b)) and scratches (Fig. 23(c)) were observed. This explains the presence of Al in the wear track as revealed by EDS analysis. The presence of hard TiC particles in the Ti_3SiC_2 matrix is possibly responsible for the wear of the Al_2O_3 ball.

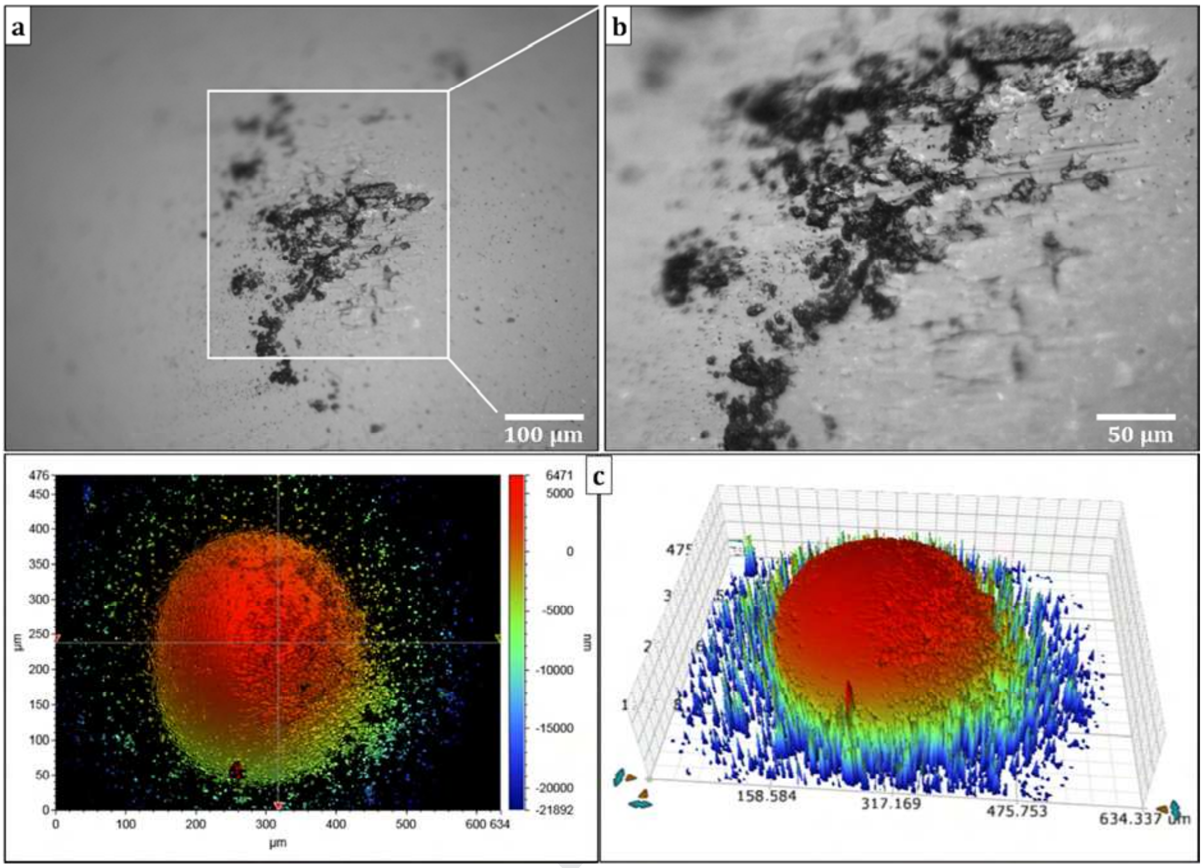

Fig. 23. Optical micrograph (a and b) and (c) 2D – to – 3D ContourGT optical surface profile of the worn surface of the Al_2O_3 ball.

5. Wear mechanisms

Following microstructural and chemical analyses before and after the wear tests, the wear mechanisms (Fig. 24) of this MAX phase composite for the test conditions are designated oxidative–deformation–reoxidation as explained thus:

5.1. Oxidative mechanism

At the beginning of the sliding contact the evolution of graphitic carbon (D and G-bands) at the sliding surface prevented the ball–to–disc contact at the asperities, thus the reduction in friction and wear in regime I. After a certain sliding time required for sufficient surface temperature build-up, oxidation of the surface induced by frictional heat further led to the subsequent evolution of anatase (TiO_2) and titanium oxycarbide (TiC_XO_Y) at the sliding surface.

5.2. Deformation mechanism

Upon repeated sliding contact, both the anatase and titanium oxycarbide tribofilm layers continues to grow until a critical thickness for spallation is reached. Since the anatase (TiO_2) part of the tribofilms is non-adherent and brittle [27], it is easily worn off. The spalled tribofilm at the sliding surface then act as abrasives to the initially formed graphitic layer, thus exposing the underlying bulk surface to wear. The contact between the ball and the disc results in grain pull-outs at the grain boundary. Consequently an abrasive three-body wear dominates the wear process, thus the transition in friction and wear (regime I– II).

5.3. *Re-oxidation mechanism*

As the sliding contact continues, the fractured grains originating from grain pull-outs are crushed and pulverized at the sliding surface. Over time, the pulverized grains become compacted and smooth enabling the reformation of the graphitic layer. Thus, a further transition from a high friction and wear regime (II) to a low friction and wear regime (III).

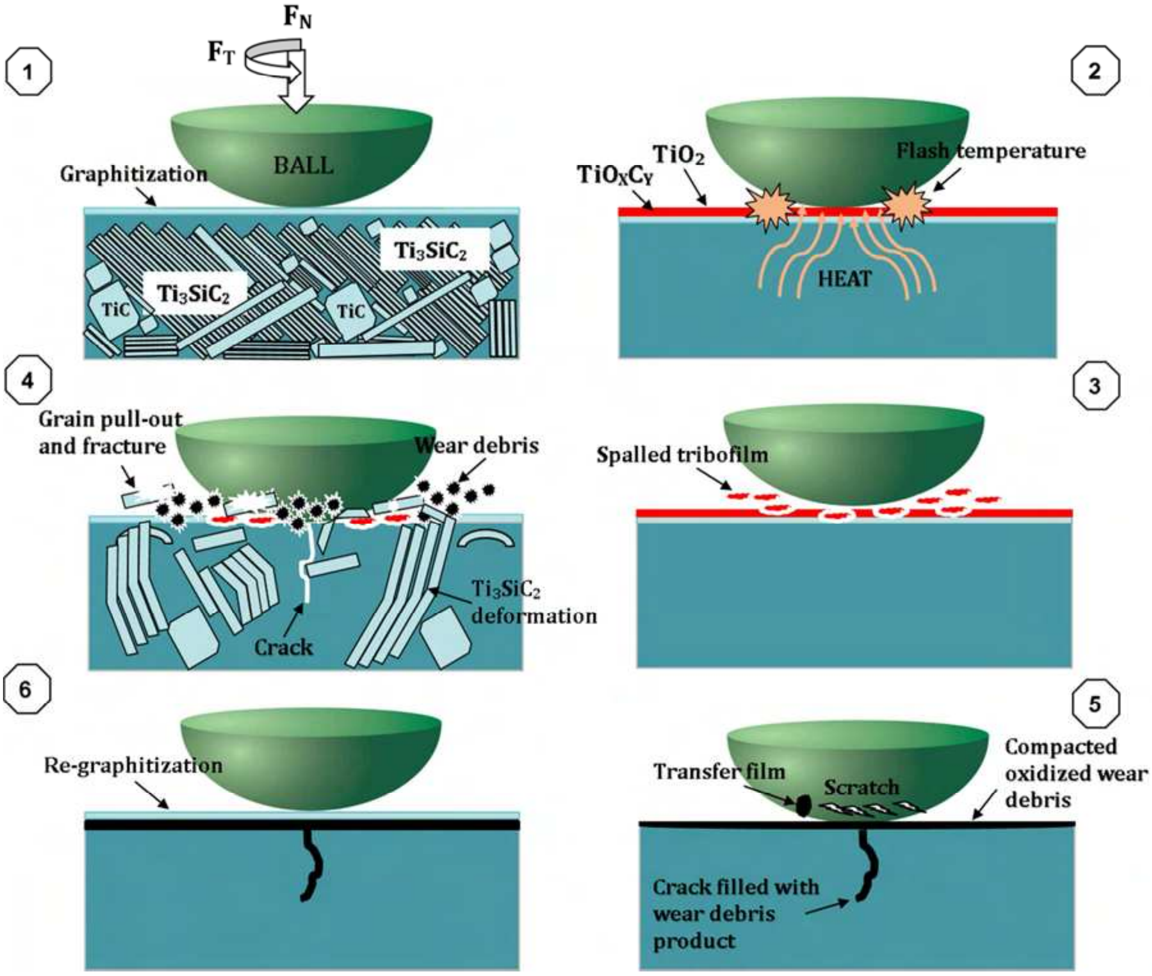

Fig. 24. Schematic presentation (1 to 6) showing the sequence of wear of the Ti_3SiC_2–$TiSi_2$–TiC MAX phase composite.

6. Conclusions

Dense polycrystalline MAX phase composite Ti_3SiC_2–$TiSi_2$–TiC was successfully synthesized by spark plasma sintering via the elemental powder route. The following conclusions can be drawn upon exhaustive characterization of the deformation microstructure and tribological behaviour of this MAX phase composite system:

1. Deformation microstructure revealed evidence of room temperature plasticity, toughening and anisotropy in mechanical response.

2. Evidence of intrinsic solid lubrication was observed due to the evolution of easy shear graphitic carbon alongside with frictional heating induced formation of anatase and titanium oxycarbide tribofilms that lubricates the sliding surface.

3. Second phase TiC particles introduce a pinning effect on the Ti_3SiC_2 grains which helps inhibit grain pull-outs as well as acting as load bearing elements— shielding the Ti_3SiC_2 grains from extensive deformation.

Acknowledgement

We wish to acknowledge the Henry Royce Institute for Advanced Materials for equipment access at Royce@sheffield.

References

1. Sloof, W.G., et al., Repeated crack healing in MAX-phase ceramics revealed by 4D in situ synchrotron X-ray tomographic microscopy. Scientific Reports, 2016. **6**: p. 23040.
2. Eklund, P., et al., The Mn + 1AXn phases: Materials science and thin-film processing. Thin Solid Films, 2010. **518**(8): p. 1851-1878.
3. Joulain, A., L. Thilly, and J. Rabier, Revisiting the defect structure of MAX phases: the case of Ti4AlN3. Philosophical Magazine, 2008. **88**(9): p. 1307-1320.
4. Barsoum, M.W. and M. Radovic, Elastic and Mechanical Properties of the MAX Phases, in Annual Review of Materials Research, Vol 41, D.R. Clarke and P. Fratzl, Editors. 2011, Annual Reviews: Palo Alto. p. 195-227.
5. Fashandi, H., et al., Synthesis of Ti3AuC2, Ti3Au2C2 and Ti3IrC2 by noble metal substitution reaction in Ti3SiC2 for high-temperature-stable Ohmic contacts to SiC. Nature Materials, 2017. **16**: p. 814.
6. Eklund, P., J. Rosen, and P.O.Å. Persson, Layered ternary Mn+1AXnphases and their 2D derivative MXene: an overview from a thin-film perspective. Journal of Physics D: Applied Physics, 2017. **50**(11): p. 113001.
7. Duan, X., et al., Synthesis of high-purity, isotropic or textured Cr2AlC bulk ceramics by spark plasma sintering of pressure-less sintered powders. Journal of the European Ceramic Society, 2015. **35**(5): p. 1393-1400.
8. Horlait, D., et al., Synthesis and Oxidation Testing of MAX Phase Composites in the Cr–Ti–Al–C Quaternary System. Journal of the American Ceramic Society, 2016. **99**(2): p. 682-690.
9. Barsoum, M.W., The MN+1AXN phases: A new class of solids: Thermodynamically stable nanolaminates. Progress in Solid State Chemistry, 2000. **28**(1): p. 201-281.

10. El-Raghy, T., et al., Processing and Mechanical Properties of Ti3SiC2: II, Effect of Grain Size and Deformation Temperature. Journal of the American Ceramic Society, 1999. **82**(10): p. 2855-2860.
11. Kronenberg, A.K., S.H. Kirby, and J. Pinkston, Basal slip and mechanical anisotropy of biotite. Journal of Geophysical Research: Solid Earth, 1990. **95**(B12): p. 19257-19278.
12. Barsoum, M.W., MAX phases : properties of machinable ternary carbides and nitrides. 2013: Weinheim, Germany : Wiley-VCH Verlag GmbH & Co. KGaA, 2013.
13. El-Raghy, T., et al., Damage mechanisms around hardness indentations in Ti□SiC□. Journal of the American Ceramic Society, 1997. **80**(2): p. 513-516.
14. Zhang, Z.-F., Z.-M. Sun, and H. Hashimoto, Deformation and fracture behavior of ternary compound Ti3SiC2 at 25–1300 °C. Materials Letters, 2003. **57**(7): p. 1295-1299.
15. Chen, D., et al., Cyclic fatigue-crack growth and fracture properties in Ti3SiC2 ceramics at elevated temperatures. Journal of the American Ceramic Society, 2001. **84**(12): p. 2914-2920.
16. Drouelle, E., et al., Deformation mechanisms during high temperature tensile creep of Ti3AlC2 MAX phase. Journal of Alloys and Compounds, 2017. **693**: p. 622-630.
17. Barsoum, M.W., et al., Fully reversible, dislocation-based compressive deformation of Ti3SiC2 to 1 GPa. Nat Mater, 2003. **2**(2): p. 107-111.
18. Molina-Aldareguia, J.M., et al., Kink formation around indents in laminated Ti 3SiC 2 thin films studied in the nanoscale. Scripta Materialia, 2003. **49**(2): p. 155-160.
19. Low, I.M., Vickers contact damage of micro-layered Ti3SiC2. Journal of the European Ceramic Society, 1998. **18**(6): p. 709-713.
20. Kooi, B.J., et al., Ti 3SiC 2: A damage tolerant ceramic studied with nano-indentations and transmission electron microscopy. Acta Materialia, 2003. **51**(10): p. 2859-2872.
21. Barsoum, M.W. and T. El-Raghy, Synthesis and Characterization of a Remarkable Ceramic: Ti3SiC2. Journal of the American Ceramic Society, 1996. **79**(7): p. 1953-1956.
22. M.W. Barsoum, H.I.Y., I.K. Polushina, V.Y. Rud, Y.V. Rud, and T. El-Raghy, Electrical conductivity, thermopower, and Hall effect of Ti3AlC2, Ti4AlN3, and Ti3SiC2. Phys. Rev, 2000. **62**(15): p. 10194-10198
23. Barsoum, M. and M. Radovic, Mechanical Properties of the MAX Phases. Vol. 41. 2011. 195-227.
24. Wang, H.-z., et al., Tribological Performance and Lubrication Mechanism of Alkylimidazolium Dialkyl Phosphates Ionic Liquids as Lubricants for Si 3 N 4 -Ti 3 SiC 2 Contacts. Vol. 2014. 2014. 1-8.
25. Wu, L., et al., Reciprocating friction and wear behavior of Ti3AlC2 and Ti3AlC2/Al2O3 composites against AISI52100 bearing steel. Wear, 2009. **266**(1): p. 158-166.
26. Lapauw, T., et al., A new method to texture dense Mn+1AXn ceramics by spark plasma deformation. Scripta Materialia, 2016. **111**(Supplement C): p. 98-101.
27. Gupta, S. and M.W. Barsoum, On the tribology of the MAX phases and their composites during dry sliding: A review. Wear, 2011. **271**(9–10): p. 1878-1894.
28. Dang, W., et al., Influence of Cu on the mechanical and tribological properties of Ti3SiC2. Ceramics International, 2016. **42**(8): p. 9972-9980.
29. El-Raghy, T., P. Blau, and M.W. Barsoum, Effect of grain size on friction and wear behavior of Ti3SiC2. Wear, 2000. **238**(2): p. 125-130.
30. Souchet, A., et al., Tribological duality of Ti3SiC2. Tribology Letters, 2005. **18**(3): p. 341-352.
31. Yanchun, Z. and S. Zhimei, Electronic structure and bonding properties in layered ternary carbide Ti3SiC2. Journal of Physics: Condensed Matter, 2000. **12**(28): p. 457.
32. Yang, J., et al., Friction and wear properties of in situ (TiB2+TiC)/Ti3SiC2 composites. Wear, 2011. **271**(11): p. 2940-2946.
33. Dang, W., et al., The tribological properties of Ti3SiC2/Cu/Al/SiC composite at elevated temperatures. Tribology International, 2016. **104**: p. 294-302.
34. Konoplyuk, S., et al., Synthesis of Ti3SiC2/TiC composites from TiH2/SiC/TiC powders. Materials Letters, 2005. **59**(18): p. 2342-2346.
35. Gupta, S., et al., Tribological behavior of select MAX phases against Al2O3 at elevated temperatures. Wear, 2008. **265**(3): p. 560-565.

36. Kero, I., R. Tegman, and M.-L. Antti, Phase reactions associated with the formation of Ti3SiC2 from TiC/Si powders. Ceramics International, 2011. **37**(7): p. 2615-2619.
37. Sato, F., J. Li, and R. Watanabe, Reaction Synthesis of Ti3SiC2 from Mixture of Elemental Powders. Vol. 41. 2000. 605-608.
38. Hashimoto, H., et al., Synthesis of Ti3SiC2 from powder blend of Ti, Si and TiC. Journal of Alloys and Compounds, 2006. **426**: p. 263-267.
39. Wu, E., et al., Intermediate Phases in Ti3SiC2 Synthesis from Ti/SiC/C Mixtures Studied by Time-Resolved Neutron Diffraction. Journal of the American Ceramic Society, 2002. **85**(12): p. 3084-3086.
40. Pang, W.K., et al., 15 - Phase and thermal stability in Ti3SiC2 and Ti3SiC2/TiC/TiSi2 systems, in Advances in Science and Technology of Mn+1axn Phases. 2012, Woodhead Publishing. p. 389-413.
41. Pang, W.K., et al., Effect of Vacuum Annealing on the Thermal Stability of Ti3SiC2/TiC/TiSi2 Composites. Journal of Australian Ceramic Society, 2009. **45**: p. 72-77.
42. Counihan, P.J., A. Crawford, and N.N. Thadhani, Influence of dynamic densification on nanostructure formation in Ti5Si3 intermetallic alloy and its bulk properties. Materials Science and Engineering: A, 1999. **267**(1): p. 26-35.
43. Lis, J., et al., Ti3SiC-based materials prepared by HIP-SHS techniques. Materials Letters, 1995. **22**(3): p. 163-168.
44. Magnus, C. and W.M. Rainforth, Influence of sintering environment on the spark plasma sintering of Maxthal 312 (nominally-Ti3SiC2) and the role of powder particle size on densification. Journal of Alloys and Compounds, 2019. **801**: p. 208-219.
45. Magnus, C. and W.M. Rainforth, Spark plasma sintering (SPS) synthesis and tribological behaviour of MAX phase composite of the family Tin+1SiCn (n = 2). Wear, 2019. **438-439**: p. 203062.
46. S. B. Li, J.X.X., L. T. Zhang & L. F. Cheng, Synthesis and some properties of Ti3SiC2 by hot pressing of Ti, Si and C powders Part 2 – Mechanical and other properties of Ti3SiC2. Materials Science and Technology, 2005. **21**(9): p. 1054-1058.
47. Magnus, C., J. Sharp, and W.M. Rainforth, The Lubricating Properties of Spark Plasma Sintered (SPS) Ti3SiC2 MAX Phase Compound and Composite. Tribology Transactions, 2019: p. 1-14.
48. Sun, Z.M., Progress in research and development on MAX phases: a family of layered ternary compounds. International Materials Reviews, 2011. **56**(3): p. 143-166.
49. Xu, J., et al., Synergistic toughening of hard, nacre-mimetic MoSi2 coatings by self-assembled hierarchical structure. Vol. 4. 2014. 4239.
50. Sun, Z., et al., Ternary Compound Ti3SiC2: Part II. Deformation and Fracture Behavior at Different Temperatures. Materials transactions, 2002. **43**(3): p. 432-435.
51. Barsoum, M. and T. El-Raghy, Room-temperature ductile carbides. Metallurgical and Materials Transactions A, 1999. **30**(2): p. 363-369.
52. Barsoum, M.W., L. Farber, and T. El-Raghy, Dislocations, kink bands, and room-temperature plasticity of Ti3SiC2. Metallurgical and Materials Transactions A, 1999. **30**(7): p. 1727-1738.
53. Frank, F.C. and A.N. Stroh, On the Theory of Kinking. Proceedings of the Physical Society. Section B, 1952. **65**(10): p. 811-821.
54. Amer, M., et al., The Raman spectrum of Ti3SiC2. Journal of Applied Physics, 1998. **84**(10): p. 5817-5819.
55. Mercier, F., et al., Raman scattering from Ti3SiC2 single crystals. Applied Physics Letters, 2011. **98**(8): p. 081912.
56. Jonathan E. Spanier, S.G., Maher S. Amer and Michel W. Barsoum, Vibrational Behavior of the Mn+1AXn Phases from First-Order Raman Scattering (M=Ti,V,Cr, A=Si, X=C,N). Physical Review B: Condensed Matter and Materials Physics, 2005. **71**(1 (2005)).
57. Jauberteau, I., et al., Silicides and Nitrides Formation in Ti Films Coated on Si and Exposed to (Ar-N2-H2) Expanding Plasma. Vol. 7. 2017. 23.
58. El-Raghy, T. and M.W. Barsoum, Diffusion kinetics of the carburization and silicidation of Ti3SiC2. Journal of Applied Physics, 1998. **83**(1): p. 112-119.

HIGHLIGHTS:

- Spark plasma sintering (SPS) was used to synthesize fully dense MAX phase composite Ti_3SiC_2-$TiSi_2$-TiC from elemental powders
- Dry-sliding friction and wear test was carried out using a pin-on-disc configuration and room temperature.
- The MAX phases exhibited intrinsic self-lubricity owing to the evolution TiC, TiC_XO_Y, and graphitic carbon at the sliding surface.
- Microscale events such as grain ripplocations, kink band (KB) formation, delamination, cavitation and grain buckling played an important role in the wear process.
- TiC acts as a load bearing element by decentralizing the sliding load via plastic deformation, as well as introducing pinning effect of the Ti_3SiC_2 grains to inhibit deformation and grain pull-outs

DECLARATION OF INTEREST STATEMENT

We have no conflict of interest to disclose.